

# Position and Orientation Control for Hyper-elastic Multi-segment Continuum Robots

Jialei Shi, *Student Member, IEEE*, Sara-Adela Abad, *Member, IEEE*, Jian S Dai, *Fellow, IEEE*, and Helge A. Wurdemann, *Member, IEEE*

**Abstract**—Elastomer-based soft continuum robots with an extensible backbone exhibit high flexibility. These manipulators might show non-linear kinematic behaviours due to, for example, the material hyper-elasticity and means of actuation. Formulating a reliable kinematic model for an effective inverse kinematics control strategy is challenging, but is paramount for allowing effective manoeuvrability and controllability. In this paper, we devise a kinematic modelling and control method for pneumatic-driven soft continuum robots (up to 100% elongation ratio). The method is based on the Cosserat rod model including a pressure-dependent dynamic modulus. The kinematic model and control strategy are then expressed as non-linear least-squares optimisation problems. Hence, various inverse kinematics control modes can be achieved for a multi-segment robot, e.g., tip position and orientation control of the overall robot or tip position control of each segment. Simulations and experiments are both conducted to validate the proposed method. The results highlight the high fidelity of the modelling technique and the effectiveness of the proposed inverse kinematics controller. In particular, the modelling and trajectory control errors for a two-segment robot are smaller than 4.5 mm, i.e., 5% of the robot's overall length.

**Index Terms**—Fluidic-driven soft robots, kinematics modelling, inverse kinematics control, position and orientation control.

## I. INTRODUCTION

CONTINUUM robots are fundamentally different from conventional robots composed of finite rigid links and joints. Instead, they have curvilinear structures with infinite elastic joints [1]. Continuum robots offer continuous deformation and are highly flexible, which is advantageous in applications involving confined spaces. Prominent examples are concentric tubes and steerable catheters for minimally invasive surgery [2]. Moreover, leveraging soft materials to construct elastomer-based continuum robots can further enhance robots' inherent compliance and flexibility, achieve safer robot-environment interactions [3] and variable stiffness

This work is supported by the Springboard Award of the Academy of Medical Sciences (grant number: SBF003-1109), the Engineering and Physical Sciences Research Council (grant numbers: EP/R037795/1, EP/S014039/1 and EP/V01062X/1), the Royal Academy of Engineering (grant number: IAPP18-19-264), the UCL Dean's Prize, UCL Mechanical Engineering, and the China Scholarship Council. For the purpose of open access, the author has applied a Creative Commons Attribution (CC BY) licence to any Author Accepted Manuscript version arising. (*Corresponding author: Helge A. Wurdemann*)

Jialei Shi, Sara-Adela Abad and Helge A. Wurdemann are with the Department of Mechanical Engineering, University College London, London, UK. (e-mail: jialei.shi.19@ucl.ac.uk; h.wurdemann@ucl.ac.uk).

Sara-Adela Abad is also with the Institute for Applied Sustainability Research, Quito, Ecuador. (e-mail: s.abad-guaman@ucl.ac.uk);

Jian S Dai is with the Institute of Robotics, Southern University of Science and Technology, Shenzhen, China and with the Centre for Robotics Research, Department of Engineering, King's College London, London, UK (e-mail: jian.dai@kcl.ac.uk).

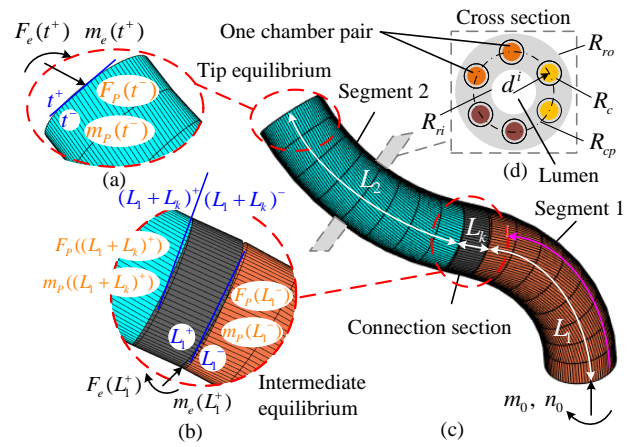


Fig. 1. Illustration of a two-segment robot: (a) Tip equilibrium at the tip of Segment 2. (b) Intermediate equilibrium at the tip of Segment 1. (c) Segment 1 (bottom module) and Segment 2 (top module). (d) Cross-sectional view. Three chamber pairs are distributed evenly with an angle of 120°.

behaviour [4]. Soft materials used for fabrication, e.g., silicone materials, have elastic moduli in the order of  $10^2 \sim 10^6$  Pa [5], with substantial stretch capabilities. Motion is commonly generated through fluidic actuation [6], [7]. However, tendon-driven [8] and hybrid-actuated methods [9], [10] also exist. To utilise the intrinsic flexibility of these soft continuum robots and enhance their controllability, addressing challenges in modelling and controlling their configuration and behaviour is of paramount importance [1]. Various kinematics, kinetics and dynamics models have been established. Kinematics studies the relationship between continuum robots' actuation space and task space without considering any forces causing the motion. Forward kinematics refers to the use of kinematic equations to obtain position and orientation of robots from parameters in the actuation space. Inverse kinematics, on the other hand, determines actuation parameters to achieve desired target poses [11]. Kinetics studies forces and torques that generate motion [12]. Dynamics combines kinematics and kinetics and studies equations of motion and time-varying forces and torques that produce any motion [8].

Continuum robots are infinite dimensional systems. Discretisation of continuum robotic structures can be considered to reduce the dimensional complexity, for instance, by utilising the Finite-Element Method (FEM) [12], [13]. In FEM, soft robots are often represented using nodes connected by elements. Commercially available software packages such as Abaqus and ANSYS [14] ease the application of FEM.

In particular, the SOFA has been developed, which delivers full-order or reduced-order simulation for soft robots using FEM [15]. Some analytical kinematic models for soft continuum robots are based on spatial curve or beam/rod models. A prominent modelling technique is the piecewise constant curvature (PCC) model. The robot shape is described by three parameters, i.e., the curve length, curvature and out-of-plane angle [11]. It is worth noting that it might be feasible here to express the configuration of articulated and continuum soft robots with classic rigid-bodied robot approaches, e.g., using Denavit–Hartenberg parameters [4], [16], [17] or augmented rigid-body models [18]–[20]. However, the constant curvature assumption might reach limitations when robots interact with the environment or external loads are applied to the robots. To this end, variable curvature models have been explored. For instance, a robot shape can be re-constructed by curve parameterisation [21]. The Cosserat rod theory can be applied to formulate the kinematics of soft robots with variable curvatures by a set of ordinary differential equations (ODEs) [22]. Strain-based Cosserat approaches have been developed to model soft robots with variable curvatures, e.g., the piecewise constant or variable strain methods [8], [23].

Utilising the aforementioned modelling methods, inverse kinematics or dynamics control has been studied. An FEM-based method was proposed in [24] to achieve inverse kinematics control of continuum robots by solving optimisation problems using SOFA. The analytical Jacobian matrix of the PCC model can be derived directly [25]. The obtained Jacobian matrix provides an explicit projection between the actuation space and the task space [26]. A kinematic curvature control method was proposed in [27] to drive a multi-segment robot to follow desired trajectories based on the PCC assumption. Continuation work for dynamic motion control was presented in [19]. In [28], inverse dynamics control was investigated to regulate the in-plane Cartesian impedance and achieve trajectory following for soft robots. Furthermore, a kinematic position control method was proposed in [29], where two robot segments are designed to have an opposite-bending-and-stretching structure, however, at the cost of sacrificing the dexterity of the robot. Furthermore, based on the Cosserat rod theory, geometric Jacobian matrices can be derived analytically or numerically [30], which are then used to achieve inverse kinematics control for soft robots with variable curvatures. A Jacobian-based inverse kinematics control method was proposed in [31] to achieve dexterous navigation for continuum robots, considering both position and orientation. These approaches can also achieve stiffness control for soft continuum robots [4] or stiffness/motion control for articulated soft robots [16], [32], [33]. In addition, the robot Jacobian [34], [35] or direct mapping between the actuation and joint spaces [36] can be obtained via learning methods. Another kinematic modelling and inverse control method for a two-segment planar soft robot was proposed in [37], considering variable curvatures and tip loads. The kinematic model was established on the absolute nodal coordinate formulation. It is noteworthy that model-based control approaches can also induce potential drawbacks. In particular, inverse dynamics methods require higher-order derivatives

of dynamics terms. Moreover, closed-loop control can be implemented to improve the accuracy of the inverse kinematics or dynamics control for soft continuum robots by introducing feedback information [13], [18]. The model-free control was used for continuum robots based on the adaptive Kalman filter that generated a robust control [38]. Here, the sensing devices will increase the cost of the robots, and it might be difficult to install additional sensors on soft robots.

Overall, modelling and control methods for soft continuum robots have been extensively developed. For elastomer-based soft robots, however, with elongation capabilities of larger than 50% *w.r.t* the original length of the robot, kinematic non-linearities (i.e., the elongation or bending motion of the robots are non-linear as a function of the actuation variables) are non-negligible. To describe these non-linearities and achieve model-based inverse kinematics control without requiring feedback loops remains challenging. Therefore, we propose a position and orientation control for hyper-elastic multi-segment continuum robots. Our contributions are:

- a static kinematic modelling and control method for pneumatic-driven, elastomer-based soft continuum robots with an extensible backbone. In particular, the forward kinematics modelling and inverse kinematics control are unified into non-linear least-squares problem by solving the ODEs from the static Cosserat rod model (see Section II-B~II-D).
- a pressure-dependent dynamic modulus to construct the stiffness density matrix of the soft robots to capture the kinematic non-linear behaviour, exclusively using a linear constitutive model (see Section II-E).
- multiple inverse kinematics control modes that do not require feedback information of robots' position and orientation. For instance, our controller can realise position and orientation control of the overall tip of a two-segment robot as well as decoupled position control of the tip of each segment, and our approach is validated through experiments using one- and two-segment soft continuum robots (see Section IV).

Section II presents the methodology of the forward kinematics model and inverse kinematics control, based on a pressure-dependent dynamic modulus. The unified non-linear least-squares problems are explained and formulated in detail. Section III describes the robot fabrication process, parameter identification and demonstrates the efficacy of the forward kinematics model using one- and two-segment robots. Section IV reports on the experimental results for the inverse kinematics control. The discussions and reflections are presented in Section V, and the conclusion is in Section VI.

## II. KINEMATIC MODELLING AND CONTROL METHOD

### A. Overview of the Robot Geometry

The soft robot used in this paper is pneumatic-driven made of highly deformable elastomer [Ecoflex 00-50 Supersoft, SmoothOn]. The design and fabrication for this robot, commonly referred to as the STIFF-FLOP manipulator [10], are detailed in Section III-A. Applications in minimally invasive surgery include colorectal surgery [10] or cancer imaging [13].

The robot has three reinforced circular chamber pairs and a free central lumen (see Fig. 1). By actuating different chamber pairs, the robot can achieve omni-directional bending ( $> 180^\circ$ ) and elongation (up to 100%).

### B. Kinematic Model

Fig. 1 shows an illustration of the soft robotic manipulator with two segments. The cross-sectional view shows that each segment has three fibre-reinforced actuation chamber pairs and a free central lumen. The subscript  $j \in \{1, 2\}$  is used to denote the index of the robot segments. For instance,  $[\cdot]_1$  is the description  $[\cdot]$  of the first segment. The air pressure inside each chamber can be described by  $[P^i]_j$ .  $i \in \{1, 2, 3, 4, 5, 6\}$  denotes the number of chambers in a one-segment robot. In particular,  $[P^1]_j = [P^2]_j$ ,  $[P^3]_j = [P^4]_j$  and  $[P^5]_j = [P^6]_j$ , as two adjacent chambers are internally connected. The robot length of each segment is denoted by  $L_1$  and  $L_2$ .

1) *Model of each Soft Robotic Segment:* Based on the Cosserat rod model [22], the spatial configuration of a soft segment can be described using a displacement vector  $p(s)$  and a rotation matrix  $R(s)$ . Their differentiation with respect to the curve length  $s$ , denoted by  $(\cdot)_s$ , is described by (1).

$$[p_{,s}(s)]_j = [R(s)v(s)]_j, \quad [R_{,s}(s)]_j = [R(s)\hat{u}(s)]_j, \quad (1)$$

where  $s \in [0, L_1]$  or  $\in [0, L_2]$ .  $v(s)$  and  $u(s)$  are the local strain vectors and curvatures.  $(\hat{\cdot})$  is the mapping from  $\mathbb{R}^3$  to  $\mathfrak{so}(3)$  [22], and its inverse operation is  $(\hat{a})^\vee = a$ . The derivatives of force  $n(s)$  and moment  $m(s)$  are in (2).

$$\begin{aligned} [n_{,s}(s)]_j &= [-f_e(s) + f_P(s)]_j, \\ [m_{,s}(s)]_j &= [-\hat{p}_{,s}(s)n(s) - l_e(s) + l_P(s)]_j. \end{aligned} \quad (2)$$

$f_e(s)$  and  $l_e(s)$  are the distributed external force and moment.  $f_P(s)$  and  $l_P(s)$  are the distributed force and moment resulting from pressurisation and are described in (3).

$$\begin{aligned} [f_P(s)]_j &= [\sum_{i=1}^6 P^i A_c R_{,s}(s) e_3^T]_j, \quad [m_P(s)]_j = \\ &[\sum_{i=1}^6 P^i A_c R(s)((v(s) + \hat{u}(s)d^i) \times e_3^T + \hat{d}^i \hat{u}(s)e_3^T)]_j. \end{aligned} \quad (3)$$

$A_c$  is the area of the cross-section of each chamber,  $\hat{d}^i$  is the position vector of the  $i$ th chamber in the body frame,  $e_3 = [0, 0, 1]$ . A linear constitutive material model is adopted to relate  $n(s), m(s)$  to  $v(s), u(s)$  and described in (4).

$$[n(s)]_j = [R(s)K_{se}(v(s) - e_3^T)]_j, \quad [m(s)]_j = [R(s)K_{bt}u(s)]_j. \quad (4)$$

$K_{se} = \text{diag}[GA, GA, EA]$ , which is the stiffness density matrix for shear and elongation. The shear modulus is  $G$ .  $K_{bt} = \text{diag}[EI_x, EI_y, GJ_z]$ , which is the stiffness density matrix for bending and twisting.  $I_x, I_y$  and  $J_z$  are the second moment of area around the  $x, y$  and  $z$ -axes and calculated in (5).

$$\begin{aligned} I_x &= \pi(R_{ro}^4 - R_{ri}^4)/4 - \sum_{i=1}^6 (\pi R_c^4/4 + |d^i|_x^2 \pi R_c^2) = I_y, \\ J_z &= \pi(R_{ro}^4 - R_{ri}^4)/2 - \sum_{i=1}^6 (\pi R_c^4/4 + |d^i|^2 \pi R_c^2). \end{aligned} \quad (5)$$

$|d^i|$  is the length of the vector  $d_i$ , and  $|d^i|_x$  is the projected length of  $d_i$  onto the  $x$ -axis.  $I_x = I_y$  results from three chamber pairs distributed evenly (see Fig. 1). The cross-sectional area of the robotic segment is calculated by  $A = \pi(R_{ro}^2 - R_{ri}^2 - 6R_c^2)$ .  $R_{rc}, R_{ri}$  and  $R_c$  are the radii of the robot, the central channel and the chamber, respectively. As both segments have the same cross-sectional geometries, the subscript  $j$  is dropped, e.g., for  $I_x, I_y, J_z$  and  $A$ .

2) *Model of the Rigid Connection Section:* The connection section/link between two robotic segments has a length of  $L_k$  and is assumed to be rigid. Similar to (1), the kinematic ODEs are simplified in (6).

$$[p_{,s}(s)]_k = [R(s)e_3^T]_k, \quad [R_{,s}(s)]_k = [R(s)[0, 0, 0]^T]_k, \quad (6)$$

where  $s \in [0, L_k]$ . The force and moment balance are detailed in (7).

$$[n_{,s}(s)]_k = [-f_e(s)]_k, \quad [m_{,s}(s)]_k = [-\hat{p}_{,s}(s)n(s) - l_e(s)]_k, \quad (7)$$

where  $[f_e(s)]_k = \rho_k A_k(s)g$  and  $[l_e(s)]_k = [0, 0, 0]^T$ , with the density of the rigid connection of  $\rho_k$ , the cross-sectional area of  $A_k(s)$ , and the  $3 \times 1$  gravity vector of  $g$ .

### C. Definition of Boundary Conditions

Boundary conditions includes the force and moment equilibrium at the intermediate connection section between two segments and the manipulator's tip (see Fig. 1). The kinematic continuity across the connection section must be satisfied.

1) *Tip Boundary Conditions:* If a manipulator is made of two segments that are of length  $L_1$  and  $L_2$ , the two-segment robot has a total length of  $L_1 + L_k + L_2$ . The boundary conditions at the manipulator's tip are reported in (8).

$$n(t^-) = F_P(t^-) + F_e(t^+), \quad m(t^-) = m_P(t^-) + m_e(t^+). \quad (8)$$

The superscripts  $-$  and  $+$  denote the left and right limits.  $F_e(t^+)$  and  $m_e(t^+)$  are the external applied tip force and moment.  $F_P(t^-)$  and  $m_P(t^-)$  are the total pressurisation force and moment at the manipulator's tip as presented in (9).

$$\begin{aligned} F_P(t^-) &= R(t) \sum_{i=1}^6 A_c [P^i]_j e_3^T, \\ m_P(t^-) &= R(t) \sum_{i=1}^6 d^i \times A_c [P^i]_j e_3. \end{aligned} \quad (9)$$

$t = L_1$  or  $t = L_2$ ,  $j = 1$  or  $j = 2$  for a one-segment robot.  $t = L_1 + L_k + L_2$  and  $j = 2$  for a two-segment robot.

2) *Intermediate Boundary Conditions:* Considering a rigid connection between two robot segments with an applied force  $F_e(L_1^+)$  and a moment  $m_e(L_1^+)$  at the end of  $L_1$ , the intermediate boundary conditions in (10) must be satisfied.

$$\begin{aligned} n(L_1^-) &= F_P(L_1^-) + n(L_1^+) + F_e(L_1^-), \\ m(L_1^-) &= m_P(L_1^-) + m(L_1^+) + m_e(L_1^-), \\ n((L_1 + L_k)^-) &= n((L_1 + L_k)^+) - F_P((L_1 + L_k)^+), \\ m((L_1 + L_k)^-) &= m((L_1 + L_k)^+) - m_P((L_1 + L_k)^+). \end{aligned} \quad (10)$$

$F_P(L_1^-)$ ,  $m_P(L_1^-)$ ,  $F_P((L_1 + L_k)^+)$  and  $m_P((L_1 + L_k)^+)$  are derived by substituting  $L_1^-$  and  $(L_1 + L_k)^+$  into (9). The kinematic continuity is depicted by (11).

$$\begin{aligned} p(L_1^-) &= p(L_1^+), \quad R(L_1^-) = R(L_1^+), \\ p((L_1 + L_k)^-) &= p((L_1 + L_k)^+), \\ R((L_1 + L_k)^-) &= R((L_1 + L_k)^+). \end{aligned} \quad (11)$$

#### D. Problem Formulation and Inverse Kinematics Control

For a one-segment robot, the robot configuration  $(p(s), R(s))$  can be derived by integrating (1) and (2), with integration length of  $L_1$  or  $L_2$ . For a two-segment robot, the robot configuration can be derived by integrating (1), (2) and (6)-(7), with integration length of  $L_1 + L_k + L_2$ . The initial conditions are the unknown force and moment at the manipulator's base  $([n_0, m_0])$ . Hence, the shooting method can be applied, guessing the initial conditions and minimising the errors of the boundary conditions. By constructing different objective functions, the forward and inverse kinematics can be formulated as non-linear least-squares problems.

1) *Forward Kinematics:* For the forward kinematics problem, the guessing value  $g(0)$  is defined in (12).

$$g(0) = [n_0, m_0]. \quad (12)$$

Rewriting (8), the objective function of the optimisation is described in (13).

$$\begin{aligned} \min_{g(0)} \quad & \|e_n\|^2 + \|e_m\|^2 \\ \text{s.t. } & e_n = n(t^-) - F_P(t^-) - F_e(t^+), \\ & e_m = m(t^-) - m_P(t^-) - m_e(t^+), \\ & \text{Equations (10) and (11) (for the two-segment robot),} \\ & [P^i]_j \geq 0 \quad (i = 1\dots 6, j = 1 \text{ and } 2). \end{aligned} \quad (13)$$

$t = L_1$  or  $t = L_2$  for a one-segment robot, and  $t = L_1 + L_k + L_2$  for a two-segment robot.

2) *Inverse Kinematics:* The control variables for our soft robot are the pressure values inside the chambers. For a one-segment manipulator, there are three pressure values inside the three chamber pairs, i.e., three degrees of freedom (DoFs) in the actuation space. A two-segment manipulator has six DoFs. For the inverse kinematics control, the initial guess  $g(0)$  includes the desired actuation pressure as defined in (14).

$$g(0) = [n_0, m_0, [P^i]_j]. \quad (14)$$

The inverse kinematics control can be summarised as follows:

**Tip position control of one segment:** Denoting the desired tip position by  $y_d^t$ , the optimisation problem becomes (15).

$$\begin{aligned} \min_{g(0)} \quad & \|e_n\|^2 + \|e_m\|^2 + \|e_t\|^2 \\ \text{s.t. } & e_n = n(t^-) - F_P(t^-) - F_e(t^+), \\ & e_m = m(t^-) - m_P(t^-) - m_e(t^+), \\ & e_t = y_d^t - p(t), \quad t = L_1 \text{ or } L_2, \\ & [P^i]_j \geq 0 \quad (i = 1\dots 6, j = 1 \text{ or } 2). \end{aligned} \quad (15)$$

**Decoupled position control of each tip of a two-segment robot:** The tip positions of Segment 1 and 2 can be controlled

independently. Denoting the desired position of the first segment  $y_d^k$ , the optimisation problem can be described as in (16).

$$\begin{aligned} \min_{g(0)} \quad & \|e_n\|^2 + \|e_m\|^2 + \|e_k\|^2 + \|e_t\|^2 \\ \text{s.t. } & e_n = n(t^-) - F_P(t^-) - F_e(t^+), \\ & e_m = m(t^-) - m_P(t^-) - m_e(t^+), \\ & e_k = y_d^k - p(L_1), \\ & e_t = y_d^t - p(t), \quad t = L_1 + L_k + L_2, \\ & [P^i]_j \geq 0 \quad (i = 1\dots 6, j = 1 \text{ and } 2), \\ & \text{Equations (10) and (11).} \end{aligned} \quad (16)$$

#### Tip position/orientation control of a two-segment robot:

The position and orientation of the overall tip of the robot are controlled. Denoting the desired tip orientation by  $R_d^t$ , the optimisation problem is formulated in (17).

$$\begin{aligned} \min_{g(0)} \quad & \|e_n\|^2 + \|e_m\|^2 + \|e_t\|^2 + \|e_R\|^2 \\ \text{s.t. } & e_n = n(t^-) - F_P(t^-) - F_e(t^+), \\ & e_m = m(t^-) - m_P(t^-) - m_e(t^+), \\ & e_t = y_d^t - p(t), \\ & e_R = (R(t)^T R_d^t - (R_d^t)^T R(t))^\vee, \quad t = L_1 + L_k + L_2, \\ & [P^i]_j \geq 0 \quad (i = 1\dots 6, j = 1 \text{ and } 2), \\ & \text{Equations (10) and (11).} \end{aligned} \quad (17)$$

Details of constructing  $e_R$  are reported in the Supplementary Material. The Fourth-order Runge-Kutta method is used for the numerical integration. The trust-region-reflective method is adopted to achieve the iterative numerical optimisation to solve the aforementioned non-linear least-squares problems [39], with the sum of squared residual errors less than  $10^{-6}$ .

#### E. System Non-linearity Analysis and Modelling

A linear constitutive material model (see Equation (4)) is applicable when the stress-strain relation can be approximated as linear. However, the longitudinal elongation and bending motion of our robotic segments are non-linear with respect to the actuation pressure. The non-linearity primarily results from, e.g., the hyper-elasticity of the silicone material and shrinking deformation of the cross-sectional geometry.

To accommodate for the kinematic non-linearity, we introduce the equivalent dynamic modulus  $E = h(P, \lambda(P))$ , i.e. the material modulus is not constant but related to the actuation pressure  $P$  and longitudinal stretch  $\lambda$ .  $h(P, \lambda(P))$  is a non-linear function.  $h(P, \lambda(P))$  can be obtained from the experimental relation between the elongation of the robot segment and the applied pressure. Using a linear constitutive model, the pure elongation of the robot is defined in (18).

$$[\lambda(P)]_j - 1 = \frac{[\Delta l]_j}{L_j} = \frac{[F(P)]_j}{[E]_j A} = \sum_{i=1}^6 \frac{[P^i]_j A_c}{[E(P)]_j A} = \frac{[\sigma(P)]_j}{[E]_j} \quad (18)$$

$[F(P)]_j$  is the longitudinal force generated by pneumatic pressurisation and  $[\sigma(P)]_j$  is the stress. Rearranging (18) yields (19).

$$[E]_j = \frac{[\sigma(P)]_j}{[\lambda(P)]_j - 1} = h(P). \quad (19)$$

In this way, a non-linear dynamic modulus function  $h(P)$  has been obtained from the experimental elongation-pressure curve.  $h(P)$  considers the non-linear strain-stress relation using a linear constitutive model (substituting (19) into (4)). The identification procedure of  $h(P)$  is presented in Section III-D.

### III. SOFT ROBOT FABRICATION, PARAMETER IDENTIFICATION AND KINEMATICS CHARACTERISATION

#### A. Segment Fabrication

The fabrication process is summarised in Fig. 2. The green-coloured moulds are 3D-printed using Tough-2000 resin on a Formlabs printer. In Step 1, six chamber moulds are printed, consisting of three parts. The reinforcement threads are tightly wound around the assembled chamber moulds with no gaps. Step 2 involves positioning the actuation chamber moulds with the outer wall mould. Silicone material is poured into the assembly. In Step 4, the six chamber moulds are removed, and silicone material is injected into the actuation chambers using a syringe. Step 5 focuses on sealing both sides of the segment using silicone adhesive (Sil-Poxy, Smooth-on). The actuation pipes (AlteSil, Altec) have inner and outer diameters of 0.5 mm and 1 mm, respectively. In this step, adjacent chambers are connected using the 1 mm pipe. Throughout the process, the silicone is cured in an oven at 60 °C for 30 minutes. A two-segment robot consists of two segments (Segment 1 and 2) aligned in series with a rigid connection segment.

#### B. Integration and Experimental Hardware

The chamber pressure is regulated and monitored by six proportional pressure regulators (Camozzi K8P). A compressor (HYUNDAI HY5508) supplies pressurised air to the pressure regulators. An Arduino Due board controls the pressure regulators via PWM signals and receives the pressure monitored by

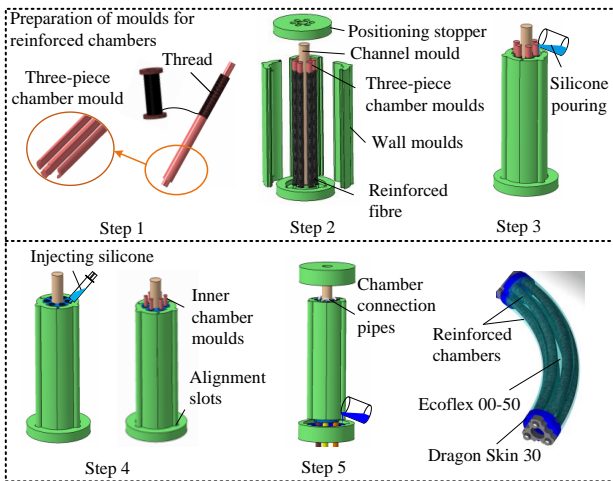


Fig. 2. Segment fabrication procedure: Step 1: 3D printing, assembling and wrapping three-piece chamber moulds using fabric thread; Step 2: Assembling all parts of the mould; Step 3: Pouring Ecoflex 00-50 into the mould; Step 4: Removing the three-piece chamber moulds. Injecting Ecoflex 00-50 into the chambers. Insertion of metal pins with a smaller diameter into actuation chambers; Step 5: Integrating actuation pipes, connecting two adjacent chambers, sealing both sides of the segment using Dragon Skin 30.

TABLE I  
IDENTIFIED SEGMENT PARAMETERS

Symbols	Description					Dimensions
	$\beta_1$	$\beta_2$	$\beta_3$	$\beta_4$	$\beta_5$	
$L_1$	Chamber length of the first segment	42.0 [mm]				
$L_2$	Chamber length of the second segment	42.0 [mm]				
$L_k$	Length of the robot connection part	5.0 [mm]				
$R_{ro}$	Radius of the segment	7.5 [mm]				
$R_{ri}$	Radius of the central channel	2.7 [mm]				
$R_{cp}$	Radius of the positioned chamber	5.1 [mm]				
$R_c$	Radius of the chamber	1.25 [mm]				
$\alpha_1$	Angle between two adjacent chambers	56.0 [°]				
$\alpha_2$	Angle between chamber pairs	120.0 [°]				
Segment 1	1641	-13630	43460	-65410	76130	
Segment 2	8727	-44680	96630	-107400	90000	

regulators. An electromagnetic tracking system (NDI Aurora) monitors the tip position/orientation of Segment 1 and 2 via magnetic trackers. MATLAB (R2019a) is used for inverse kinematics control and data acquisition. The desired pressure is converted to a PWM signal and sent to the Arduino Due board. Details on the experimental hardware and control scheme (e.g., low-level pressure control) are reported in [40] and the Supplementary Material, respectively.

#### C. Parameter Identification/Numerical Simulation Analysis

Table I summarises the geometric parameters of one segment. To identify the parameters of the pressure-dependent dynamic modulus, the elongation-pressure relationship of two segments was measured through 5 trials (see Fig. 3(a)). The elongation was measured by the NDI tracker. Following (18) and (19), a fourth-order polynomial in (20) is fitted.

$$E = \beta_1 P^4 + \beta_2 P^3 + \beta_3 P^2 + \beta_4 P + \beta_5. \quad (20)$$

$P$  denotes the averaged pressure of the six chamber in bar. The identified coefficients  $\beta_1$ ,  $\beta_2$ ,  $\beta_3$ ,  $\beta_4$  and  $\beta_5$  are reported in Table I. The root mean square errors (RMSE) are 63.73 Pa and 35.80 Pa for Segment 1 and 2, as reported in Fig. 3(b). In this case, the RMSE values of the simulated elongation for Segment 1 and 2 are 0.24 mm and 0.22 mm, respectively.

The presented model with the identified parameters is simulated in MATLAB to determine a suitable element number.

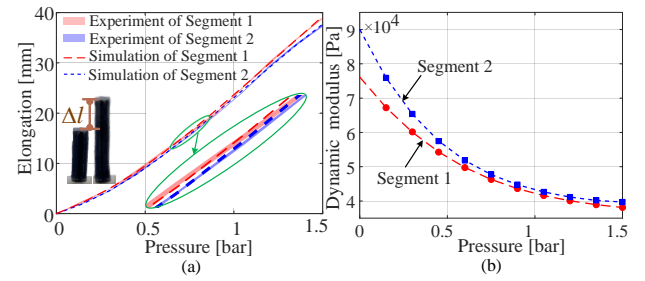


Fig. 3. (a) The experimental and analytical elongation results for Segment 1 and 2. The shaded red and blue areas indicate a small variability of the experimental results for the elongation. (b) The identified dynamic modulus of Segment 1 and 2 using a fourth-order polynomial with respect to the averaged actuation pressure  $P$  (see Equation (20)).

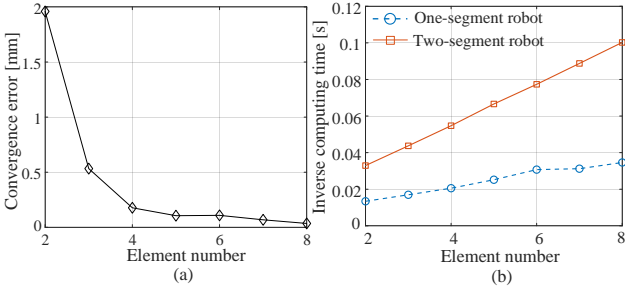


Fig. 4. (a) Convergence error of the tip position in the Cartesian space for a one-segment robot with increasing element number. (b) Computational time of the inverse kinematics control for a one- and two-segment robot as the number of elements increases.

A larger number of elements improves the model's accuracy; however, increasing the number of elements yields a higher computational burden. Fig. 4(a) illustrates the convergence error of the tip position for a one-segment robot as the element number increases. The position error converges to below 0.10 mm for more than five elements. Fig. 4(b) also demonstrates that the computational complexity scales approximately linearly with the number of elements for both one-segment and two-segment robots. The model was implemented on a PC (Intel i5, RAM 32 GB). In this paper, we chose to set the element number to 6. As such, the average inverse kinematics control frequency for a one-segment and two-segment robot can reach 33 Hz and 13 Hz, respectively.

#### D. Kinematics Characterisation and Validation

Based on the identified parameters in Section III-C, Figs. 5(a) and (b) report on the shape comparison between the computational model and experimental results for Segment 1 and 2 for three pressure levels (i.e., 0.6 bar, 1.05 bar and 1.5 bar), when both one and two chamber pairs are actuated. Figs. 5(c) and (d) detail the bending angle results when

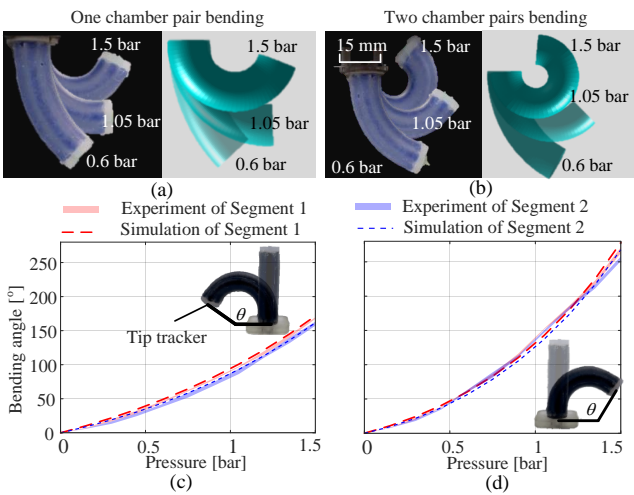


Fig. 5. Experimental and simulation bending results for one-segment robots. Segment shapes are illustrated for the actuation of (a) one and (b) two chamber pairs. Results of experimental and simulated bending angles when (c) one chamber pair is actuated and (d) two chamber pairs are actuated.

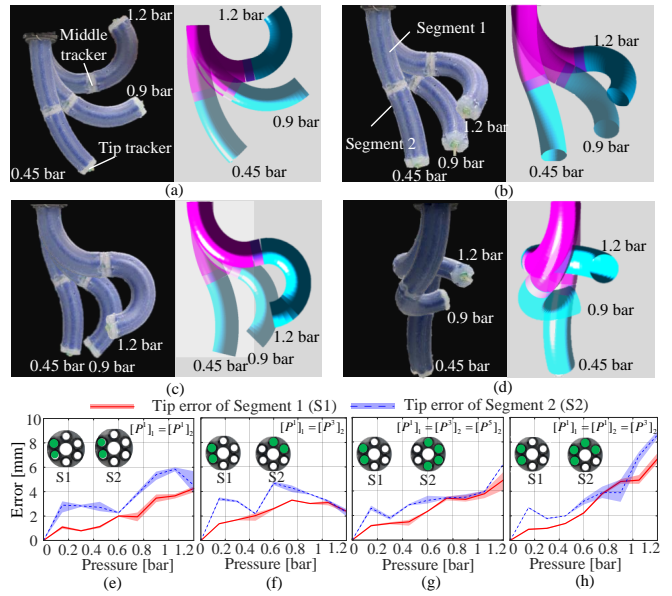


Fig. 6. Kinematics characterisation and validation results for the two-segment robot: The comparisons between the computational model and experiments when (a)  $[P^1]_1 = [P^1]_2$ , (b)  $[P^1]_1 = [P^3]_2$ , (c)  $[P^1]_1 = [P^3]_2 = [P^5]_2$ , and (d)  $[P^1]_1 = [P^1]_2 = [P^3]_2$ . The corresponding tip errors for Segment 1 and 2 are reported in (e)-(h). The actuated chambers are coloured in green.

pressure varies from 0 bar to 1.5 bar. The experimental results show that maximum bending angles of  $266.9^\circ$  and  $254.4^\circ$  are achieved for Segment 1 and 2, respectively. When one chamber pair is actuated, the RMSE values are  $3.5^\circ$  and  $2.7^\circ$  for Segment 1 and 2. Moreover, the RMSE values are  $5.3^\circ$  and  $7.1^\circ$  for Segment 1 and 2 under two chamber pairs actuation.

Fig. 6 reports on four simulated and experimental kinematic responses when Segment 1 and 2 form a two-segment robotic manipulator. Figs. 6(a) and (c) compare the robot's shape when Segment 1 and 2 bend within a plane with the same as well as opposite bending curvatures. Figs. 6(b) and (d) show the results when Segment 1 and 2 bend in different planes. The shape alignment reveals a high fidelity of our analytical model. Figs. 6(e)-(h) detail the model errors of the tip position of each segment. In particular, the overall tip RMSE values of Segment 2 are 3.76 mm (Fig. 6(e)), 3.28 mm (Fig. 6(f)), 3.45 mm (Fig. 6(g)) and 4.42 mm (Fig. 6(h)). Moreover, the corresponding RMSE values for Segment 1 are 2.46 mm, 2.38 mm, 2.82 mm and 3.56 mm.

#### IV. VALIDATION OF INVERSE KINEMATICS CONTROL FOR ONE- AND TWO-SEGMENT ROBOTS

Validation of the proposed inverse kinematics-based controller in the free-space for one-segment (Experiment 1) and two-segment robots (Experiments 2 and 3) is first conducted. In Experiment 1, a magnetic tracker is mounted at the robot's tip. In Experiment 2-3, one magnetic tracker is fixed to the overall tip of the two-segment robot (i.e., to the tip of Segment 2) in addition to a second tracker that is mounted at the midpoint of the robot (i.e., at the tip of Segment 1). In Experiment 4, tip loads are applied to the one-segment and two-segment robots to explore the efficacy of the inverse kinematics control under known external disturbances.

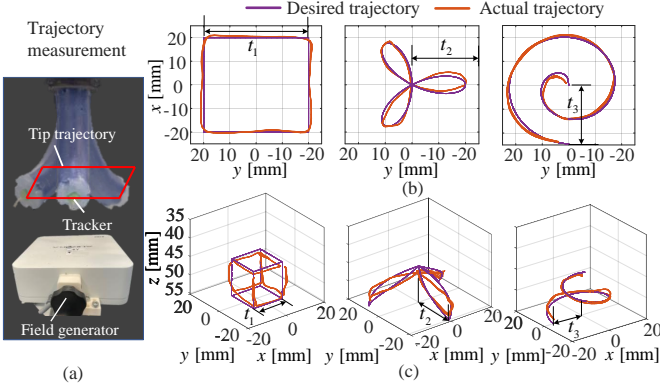


Fig. 7. Results for Experiment 1 (one-segment robot): Trajectory illustration and tracking results for six shapes. (Data are from Segment 1).  $t_1$ ,  $t_2$  and  $t_3$  are used to describe the trajectory size. (a) Trajectory measurement setup. Desired and experimental trajectories with (b) a constant height (square, elliptical, spiral) and (c) a variable height (cube, elliptical, spiral).

#### A. Experimental Protocols

##### 1) Experiment 1 - Position control of a single segment:

Segment 1 and 2 are tested over ten trials following two sets of trajectories consisting of a constant and variable height.

**Constant height:** Trajectories of three shapes (see Fig. 7(b)) are investigated, i.e., a square ( $t_1 = 30, 40$  mm), elliptical ( $t_2 = 15, 20$  mm) and spiral trajectory ( $t_3 = 18, 24$  mm). The trajectory heights are constant.

**Variable height:** Trajectories of three shapes (see Fig. 7(c)) are investigated. Again, each shape varies in size, i.e., a box ( $t_1 = 15, 20$  mm), elliptical ( $t_2 = 15, 20$  mm) and spiral trajectory ( $t_3 = 15, 21$  mm). All the trajectories have a variable height of 10 mm.

**2) Experiment 2 - Decoupled tip position control of each segment for a two-segment robot:** The tip positions of Segment 1 and 2 are controlled independently. Four trajectory combinations are investigated over ten trials:

- S20C30: The overall tip of the manipulator (i.e., the tip of Segment 2) follows a circle (30 mm radius). The midpoint of the manipulator (i.e., the tip of Segment 1) follows a square (20 mm side length).
- M0T27: The overall tip of the manipulator follows a spiral trajectory ( $t_3 = 27$  mm). The midpoint of the manipulator is stationary.
- L15T27: The overall tip of the manipulator follows a spiral trajectory ( $t_3 = 27$  mm). The midpoint of the manipulator follows a line (15 mm length).
- M12T27: The overall tip of the manipulator follows a spiral trajectory ( $t_3 = 27$  mm). The midpoint of the manipulator follows a spiral trajectory ( $t_3 = 12$  mm).

**3) Experiment 3 - Tip position and orientation control of the two-segment robot:** Two sets of experiments are investigated. Each trajectory is repeated over ten trials:

- The robot's tip is controlled to follow a box trajectory ( $t_1 = 30$  mm), elliptical trajectory ( $t_2 = 30$  mm) and a spiral trajectory ( $t_3 = 30$  mm). The trajectory height has a variation of 20 mm. Meanwhile, the tip orientation of the robot is aligned parallel to the  $z$  axis.

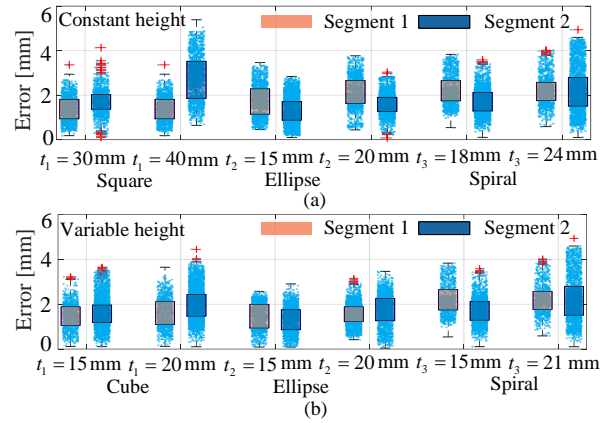


Fig. 8. Results for Experiment 1 (one-segment robot): The trajectory tracking results of the Segment 1 and 2 when the trajectory height is (a) constant and (b) variable, using a boxplot. The blue scattered points are error values.

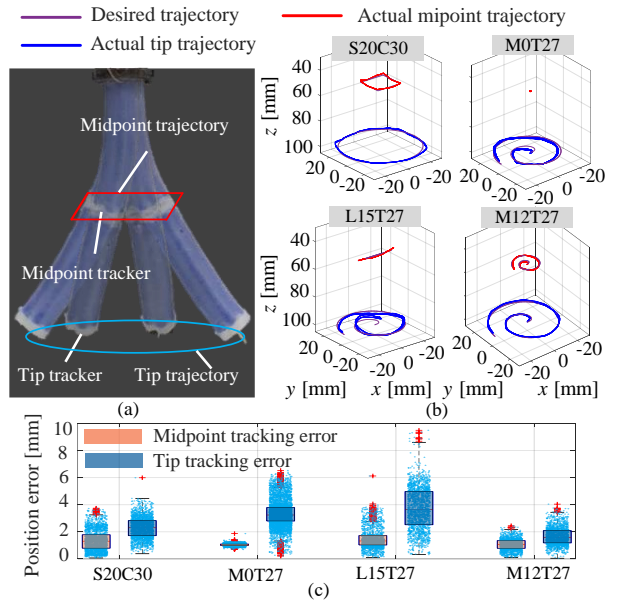


Fig. 9. Results for Experiment 2 (two-segment robot): (a) The midpoint and tip position are measured by two Aurora trackers. (b) The tracking trajectories and the results of the decoupled midpoint and tip position control. Please refer to the supplementary video for more details. (c) The summarised midpoint and tip position control errors.

- The robot's tip is controlled to follow a spiral trajectory ( $t_3 = 30$  mm), with a variable orientation but constant bending angles of  $0^\circ$ ,  $30^\circ$ ,  $45^\circ$  and  $60^\circ$ .

**4) Experiment 4 - Inverse kinematics control with known tip loads:** For the one-segment robot, 0 g, 5 g and 10 g loads are applied at the robot's tip while tracking a constant-height spiral trajectory ( $t_3 = 24$  mm) and a variable-height spiral trajectory ( $t_3 = 21$  mm, a height variation of 10 mm). For the two-segment robot, 0 g, 5 g and 10 g loads are applied at the robot's overall tip while tracking a constant-height spiral trajectory ( $t_3 = 30$  mm, a bending angle of  $0^\circ$ ).

#### B. Experimental Results

**Results for Experiment 1:** Fig. 7(a) depicts the tip trajectory measurements using an NDI field generator and a tracking

sensor at segment tip. Fig. 7(b) illustrates the square, elliptical and spiral trajectories in purple colour (constant height), compared to the actual trajectories in red colour (for Segment 1). Fig. 7(c) shows results for desired box, elliptical and spiral trajectories with a variable height. Fig. 8 summarises the absolute tracking errors for Segment 1 and 2 when trajectories have a constant height (see Fig. 8(a)) and a variable height (see Fig. 8(b)). It is observed that the tracking accuracy for Segment 1 and 2 is similar across the different trajectories, e.g., the discrepancy of the median error values of the two segments is less than 0.5 mm in all cases. The maximum tracking errors of the two segments are less than 5.0 mm. The overall median error values are between 1.40 mm and 2.89 mm, i.e., between 3.11% and 6.44% of the original robot length.

**Results for Experiment 2:** Fig. 9 reports the tracking results when the midpoint (i.e., tip of Segment 1) and tip of a two-segment manipulator (i.e., tip of Segment 2) are controlled to follow different trajectories. Fig. 9(a) illustrates that tracking sensors are embedded in the connection section and at the tip of the robot. Four desired and actual trajectory combinations are compared in Fig. 9(b). Fig. 9(c) details the tracking errors in boxplots. The median errors of the tracking sensor in the midpoint of the robotic manipulator show similar values below 1.50 mm for all four trajectory combinations. In contrast, the accuracy of the tip position varies for different trajectories. For instance, the median tip tracking errors are 2.36 mm, 3.22 mm, 3.71 mm and 1.60 mm for the S30C30, M0T27, L15T27 and M12T27 trajectories. Larger errors (e.g., up to 6.50 mm and 9.50 mm) are observed when the robot midpoint tracks a line while the robot tip tracks a spiral trajectory (see L15T27). For S30C30 and M12T27 trajectories, the maximum tip tracking errors are below 5.0 mm.

**Results for Experiment 3:** Fig. 10(a) illustrates the experiment when the robot tip follows a desired trajectory. The tip orientation remains along the  $z$ -axis, which could be useful for delicate grasping tasks or medical examination [29], [31]. Fig. 10(b) shows the desired box, elliptical and spiral trajectories of the robot's tip. Figs. 10(c)-(e) report tracking errors of the tip position and tip bending angle. It is observed that overall position errors are less than 6.0 mm with RMSE values of 2.83 mm, 2.88 mm and 3.03 mm for the box, elliptical and spiral trajectories, respectively. Given that the desired bending angle is  $0^\circ$ , RMSE values are  $3.4^\circ$ ,  $3.2^\circ$  and  $2.4^\circ$ . Fig. 11 reports the results of tip bending angle control while tracking a spiral trajectory. Fig. 11(a) illustrates experiments where the robot tip follows a same trajectory with a variety of tip bending angles of  $0^\circ$ ,  $30^\circ$ ,  $45^\circ$ , and  $60^\circ$ . The experimental bending angles are plotted in Fig. 11(b). Here, RMSE values of the tip position tracking are 2.32 mm (tracking  $0^\circ$ ), 3.34 mm (tracking  $30^\circ$ ), 2.91 mm (tracking  $45^\circ$ ) and 3.05 mm (tracking  $60^\circ$ ), as shown in Fig. 11(c). Meanwhile, the corresponding tip angle errors are  $2.0^\circ$ ,  $2.1^\circ$ ,  $2.6^\circ$  and  $3.1^\circ$ , as reported in Fig. 11(d). The angle errors tend to increase when the desired bending angles vary from  $0^\circ$  to  $60^\circ$ , with the maximum errors being smaller than  $7.0^\circ$ .

**Results for Experiment 4:** Fig. 12 reports the tracking errors for spiral trajectories while applying constant loads of (0, 5 and 10 g) at the tip of the one-segment robot. Fig. 12(a) shows

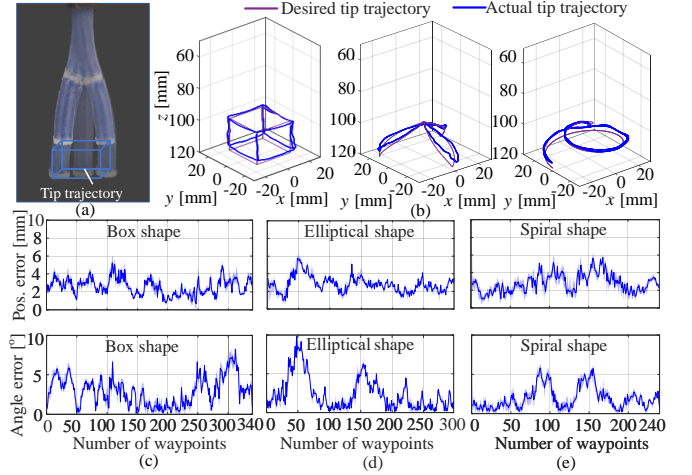


Fig. 10. Results for Experiment 3 (two segment-robot): (a) Control of tip position and orientation (remained along the  $z$ -axis). (b) Tracking results for box, elliptical and spiral trajectories. Position and orientation errors for tracking (c) the box, (d) the elliptical and (e) the spiral trajectories.

that RMSE values are 2.32 mm, 2.64 mm and 2.45 mm for loads of 0, 5 and 10 g, respectively. Fig. 12(b) illustrates the robot can be controlled to execute stable vertical motion with tip loads. RMSE values are 2.12 mm, 1.94 mm and 1.85 mm when applying 0, 5 and 10 g loads, respectively. In summary, the tracking errors remain consistent across different tip loads. Fig. 13 summarises errors of tip position and orientation control (using a constant-height spiral trajectory with a bending angle of  $0^\circ$ ) for the two-segment robot under tip loads of

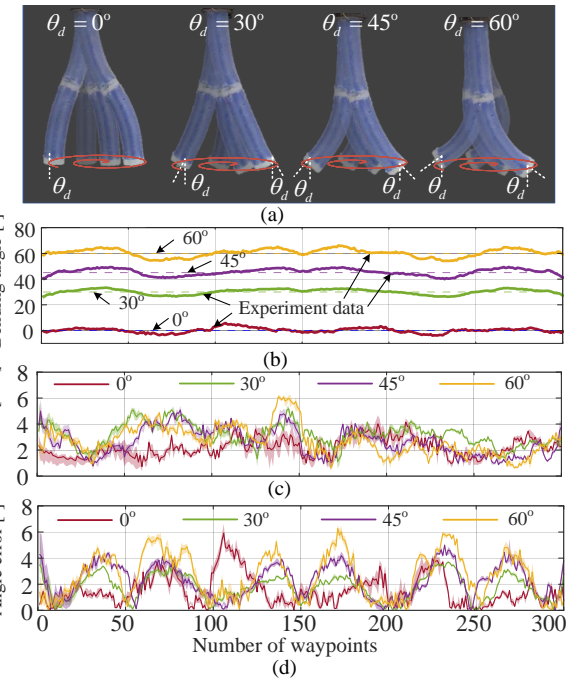


Fig. 11. Results for Experiment 3 (two-segment robot): (a) The robot tip follows a constant-height spiral trajectory ( $t_3=30$  mm), with desired bending angles of  $0^\circ$ ,  $30^\circ$ ,  $45^\circ$ ,  $60^\circ$  at the tip. (b) Experimental bending angles in one trajectory period. (c) Position tracking errors and (d) corresponding bending angle errors.

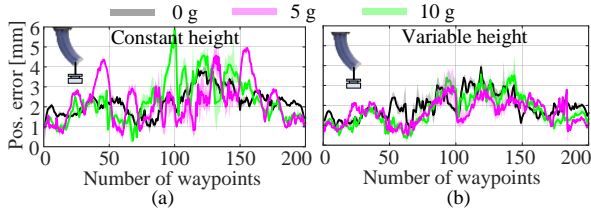


Fig. 12. Results for Experiment 4 (one-segment robot): Position (Pos.) tracking errors of a spiral trajectory for Segment 1, with tip loads of 0, 5, and 10 g. (a) The trajectory height is constant and  $t_3 = 24$  mm. (b) The trajectory height has a variation of 10 mm and  $t_3 = 21$  mm.

0, 5, and 10 g. The maximum position and bending angle errors are below 7.0 mm and 8.0°, respectively. The results demonstrate that the inverse kinematics control approach for the two-segment robot can handle known tip loads. RMSE values are between 2.0 mm ~ 3.5 mm and 1.5° ~ 2.5° for the position and bending angle control.

## V. DISCUSSIONS OF RESULTS

Experiments 1-4 demonstrate that one- and two-segment robots can both follow complex motion in 3D space, with a consideration of tip loads. The elongation capability allows the manipulator to have vertical displacements (e.g., 20 mm), without significant reduction in accuracy (see Experiment 3). It is worth mentioning that the modelling and control error might also result from properties of silicone materials such as its hysteresis. As such, the robot may exhibit kinematic discrepancies, even when subject to identical actuation pressure. Moreover, uncertainties from the parameter identification, pressure control (pressure error of 0.03 bar) and magnetic sensors (position error of 0.48 mm, bending angle error of 0.30°) contribute to the overall error. Supplementary Material provides a detailed uncertainty and sensitivity analysis. For instance, it is found that the kinematics model is most sensitive to the pressure, and the pressure uncertainty could introduce 40% ~ 60% error to the robot's tip position and bending angle.

Experiment 1 demonstrates the errors for Segment 2 have larger distributions compared to Segment 1 (see Fig. 8). One reason might be the inconsistency in the fabrication process of the segments. In fact, the variation in the identified dynamic moduli of two segments (see Fig. 3(b)) supports this hypothesis. Experiment 2 reports that the overall tip tracking errors (up to 9.5 mm) are larger than the midpoint errors (up to 6.5 mm) for a two-segment robot (see Fig. 9(c)). Another reason for the difference in error values might be the error propagation of the kinematic model primarily resulting from parameter and pressure control uncertainty (see Supplementary Material). When both tips are controlled, the control errors from Segment 1 will add to the overall tip error of the two-segment robot at the tip of Segment 2. This is also supported by the kinematics validation results in Fig. 6. Here, the overall tip errors (3~5 mm) are larger than the midpoint errors (2~4 mm). Experiment 3 reports similar tip position errors when following four tip angles. In contrast, the errors of the tip bending angle tend to be larger when desired angles increase. This might be a result of the hardware setup, e.g., Figs. 11(b)

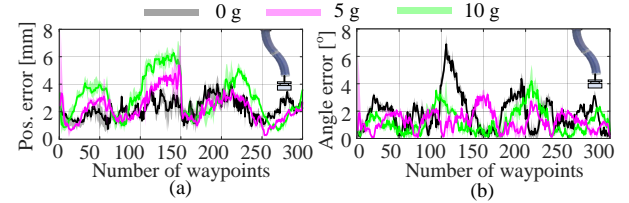


Fig. 13. Results for Experiment 4 (two-segment robot): (a) Position (Pos.) and (b) orientation tracking errors when tracking a constant-height spiral trajectory ( $t_3=30$  mm), with tip loads of 0 g, 5 g and 10 g.

and (d) show the angle errors have a similar pattern, which might be caused by the installation of the tracking sensor.

Table II summarises key performance indicators of approaches found in literature and provides a comparison. Our method achieves both position and orientation control. For position control only, our work outperforms FEM-based [13] and analytical model-based control techniques [41], [42]. Data-driven control methods however can achieve higher accuracy, thanks to a large training data [34]. The accuracy of our model-based inverse kinematics control depends on the accuracy of the kinematics model. To cope with any non-linear behaviour of elastomer-based soft robots, hyper-elastic material models can be included [43]. Increasing a kinematic model's complexity might affect the computational efficiency for inverse kinematics control. Moreover, the non-linearity might also result from the air pressurisation in each chamber pair. This effect might be challenging to capture in an analytical approach. In contrast, we defined a pressure-dependent dynamic modulus capturing the kinematic non-linearity using a linear constitutive model as in (4), without increasing the complexity of the kinematic model structure or incorporating hyper-elastic models. The results demonstrate that our kinematics model has a high fidelity (see Fig. 6). The parameter identification is based exclusively on the elongation-pressure test which is convenient to obtain. Hence, our proposed method has the potential to be applied to control a number of serial or parallel soft continuum robots in various applications, e.g., minimally invasive surgery [42], soft gripper [29], or bending manipulators [43], capturing a nonlinear strain-stress relation in their statics or dynamics models.

The computational speed varies among all approaches; our work computes at an average rate compared to other methods (see Table II). Several factors impact the computational speed of our algorithm in our work: Firstly, the number of elements was set to six resulting in satisfying control accuracy and feasible control frequency for a one- and two-segment robot between 30 ~ 50 Hz and 13 ~ 25 Hz (see Table II), when implementing our model in MATLAB running on a PC with an Intel i5 processor, 32 GB RAM. Second, the computational time increases with the number of robot segments, as reported in Fig. 4(b). For instance, the computational time of inverse kinematics is about 5 ms and 12 ms per element when the number of segments is one and two, respectively. Applying our approach to robots with more than two segments requires the consideration of intermediate conditions reported in (10) and (11). Third, the computational performance is

ato

TABLE II  
COMPARISON OF OPEN-LOOP INVERSE KINEMATICS CONTROL FOR SOFT ROBOTS BETWEEN OUR APPROACH AND EXISTING WORKS

Reference	Actuation Method	Robot Type	Inverse Kinematics Control Method	Position Accuracy	Orientation Accuracy	Computation Time (Language/Software)	Considering Hyper-elasticity
[13]	Pneumatic-driven	Multi-segment	FEM-based	7.9 mm (< 8%)	—	75 ms (SOFA)	No
[34]	Pneumatic-driven	One-segment	Learning-based	0.78 mm (< 1%)	—	28 ms (C++)	Yes
[41]	Magnetic-driven	Multi-segment	Analytical Jacobian-based	6.0 mm (< 6%)	—	133 ms (MATLAB)	No
[42]	Pneumatic-driven	Parallel Robot	Analytical Model-based	9.4 mm (< 6%)	—	3.5 ms (MATLAB)	No
Our work	Pneumatic-driven	Multi-segment	Analytical Model-based	3.4 mm (< 4%)	3.5°	77 ms (MATLAB)	Yes

\* The percentage indicates the relative position error in relation to the original length of the robot. — denotes that the orientation control is not considered.

influenced by the implementation language. A solution can be achieved within 5 optimisation iterations using MATLAB, which demonstrates the computational burden is similar to existing literature [44] showing that the 5.5 iterations cost 1.5 ms when using C++. The MATLAB Coder could be explored to generate C++ code. On average, algorithms running in C++ are estimated to require less computational time compared to using the scripting language MATLAB. Dynamic memory allocation and data visualisation might cost additional time when using MATLAB. Please note that soft robots usually have low bandwidths, e.g., 1 Hz [45]. Hence, high-frequency inverse kinematics control at kHz rates might not be required.

Our model-based, open-loop control approach does not require gathering large data sets for modelling or the integration of position and orientation sensors. In space-constrained applications, e.g., in minimally invasive surgery, size requirements of clinical settings often impede sensor implementation [1]. Experiment 4 demonstrates the effectiveness of our controller when the tip load is known. In real-world applications, however, external disturbances might be unknown, which might call for closed-loop control combining with proprioceptive and exteroceptive sensing, e.g., using PI [13], [24] or PD control [46], and robust adaptive control [38]. Our current work focuses on the statics modelling and control of soft robots, rather than the derivation of dynamic behaviour, for low-motion tasks. Performance of the proposed approach can be further enhanced by advancing the hardware and extending the contribution to include dynamics-based controllers. In our presented work, the midpoint and/or tip of the soft manipulator is constrained to achieve inverse kinematics control. When navigating soft robots in real-world environments such as inside the abdominal area for instance, it might be necessary to avoid obstacles or sensitive areas. In these cases, our approach can be enhanced by controlling or constraining a number of points along a multi-segment robot.

## VI. CONCLUSIONS

This paper presented an optimisation-based kinematic modelling and control method for hyper-elastic continuum robots. The forward kinematics and inverse kinematics control are unified into the non-linear least-squares problems. By minimising a number of objective functions, our method produces various control modes, i.e., the tip position control for a one-segment robot, the tip position and the orientation control for a two-segment robot. The concluding remarks and findings are:

- Our approach allows for a decoupled control of each segment tip of a soft continuum, multi-segment manipulator (median tracking errors are less than 2.0 mm and 4.0 mm for the tips of Segment 1 and 2, respectively). This property might be beneficial when soft robotic manipulators operate in confined spaces, e.g., a pivoting motion can be defined constraining some sections of a manipulator [31].
- Non-linear kinematic behaviour can be captured by a pressure-dependent dynamic modulus.
- The combination of our modelling and control strategies results in high fidelity and effectiveness (e.g., tip modelling with control errors for a two-segment robot are generally less than 4.5 mm, i.e., 5% of the robot length), without requiring sensing the robot's configuration.

Future work includes exploring the manipulator's dynamic behaviour and an analysis of the controller's stability. In particular, this work achieves an open-loop inverse kinematics control. Therefore, prospective work will include a stability analysis of a closed-loop control system, which may involve studying the dynamics of the continuum robots, the pressure regulation and the trajectory generator. We aim to extend our work by implementing statics or dynamics control strategies on medical applications, e.g., in-vivo cancer imaging.

## REFERENCES

- [1] J. Burgner-Kahrs, D. C. Rucker, and H. Choset, "Continuum robots for medical applications: A survey," *IEEE Trans. Robot.*, vol. 31, no. 6, pp. 1261–1280, 2015.
- [2] X. Hu, A. Chen, Y. Luo, C. Zhang, and E. Zhang, "Steerable catheters for minimally invasive surgery: A review and future directions," *Comput. Assisted Surg.*, vol. 23, no. 1, pp. 21–41, 2018.
- [3] P. Polygerinos *et al.*, "Soft robotics: Review of fluid-driven intrinsically soft devices; manufacturing, sensing, control, and applications in human-robot interaction," *Adv. Eng. Mater.*, no. 12, p. 1700016, 2017.
- [4] F. Stella, J. Hughes, D. Rus, and C. Della Santina, "Prescribing Cartesian stiffness of soft robots by co-optimization of shape and segment-level stiffness," *Soft Rob.*, vol. 10, no. 4, pp. 701–712, 2023.
- [5] C. Majidi, "Soft robotics: A perspective—current trends and prospects for the future," *Soft Rob.*, vol. 1, no. 1, pp. 5–11, 2014.
- [6] A. D. Marchese, R. K. Katzschmann, and D. Rus, "A recipe for soft fluidic elastomer robots," *Soft Rob.*, vol. 2, no. 1, pp. 7–25, 2015.
- [7] J. Peters *et al.*, "Actuation and stiffening in fluid-driven soft robots using low-melting-point material," in *Proc. IEEE/RSJ Int. Conf. Intell. Robots Syst.*, 2019, pp. 4692–4698.
- [8] F. Renda, F. Boyer, J. Dias, and L. Seneviratne, "Discrete Cosserat approach for multisection soft manipulator dynamics," *IEEE Trans. Robot.*, vol. 34, no. 6, pp. 1518–1533, 2018.
- [9] J. Peters, B. Anvari, C. Chen, Z. Lim, and H. A. Wurdemann, "Hybrid fluidic actuation for a foam-based soft actuator," in *Proc. IEEE/RSJ Int. Conf. Intell. Robots Syst.*, 2020, pp. 8701–8708.

- [10] H. A. Wurdemann, A. Stilli, and K. Althoefer, "Lecture notes in computer science: An antagonistic actuation technique for simultaneous stiffness and position control," in *Proc. Int. Conf. Intell. Robot. Autom.*, 2015, pp. 164–174.
- [11] R. J. Webster III and B. A. Jones, "Design and kinematic modeling of constant curvature continuum robots: A review," *Int. J. Rob. Res.*, vol. 29, no. 13, pp. 1661–1683, 2010.
- [12] X. Hu *et al.*, "A novel methodology for comprehensive modeling of the kinetic behavior of steerable catheters," *IEEE/ASME Trans. Mechatronics*, vol. 24, no. 4, pp. 1785–1797, 2019.
- [13] P. Chaillou *et al.*, "Reduced finite element modelling and closed-loop control of pneumatic-driven soft continuum robots," in *Proc. IEEE Int. Conf. Soft Robot.*, 2023, pp. 1–8.
- [14] C. Yang, R. Kang, D. T. Branson, L. Chen, and J. S. Dai, "Kinematics and statics of eccentric soft bending actuators with external payloads," *Mech. Mach. Theory*, vol. 139, pp. 526–541, 2019.
- [15] O. Goury and C. Duriez, "Fast, generic, and reliable control and simulation of soft robots using model order reduction," *IEEE Trans. Robot.*, vol. 34, no. 6, pp. 1565–1576, 2018.
- [16] R. Mengacci *et al.*, "On the motion/stiffness decoupling property of articulated soft robots with application to model-free torque iterative learning control," *Int. J. Rob. Res.*, vol. 40, no. 1, pp. 348–374, 2021.
- [17] J. M. Gandarias *et al.*, "Open-loop position control in collaborative, modular variable-stiffness-link (VSL) robots," *IEEE Rob. Autom. Lett.*, vol. 5, no. 2, pp. 1772–1779, 2020.
- [18] C. Wang, C. G. Frazelle, J. R. Wagner, and I. D. Walker, "Dynamic control of multisection three-dimensional continuum manipulators based on virtual discrete-jointed robot models," *IEEE/ASME Trans. Mechatronics*, vol. 26, no. 2, pp. 777–788, 2020.
- [19] R. K. Katzschmann *et al.*, "Dynamic motion control of multi-segment soft robots using piecewise constant curvature matched with an augmented rigid body model," in *Proc. IEEE Int. Conf. Soft Robot.*, 2019, pp. 454–461.
- [20] S. Yang *et al.*, "Dynamic capture using a traplike soft gripper with stiffness anisotropy," *IEEE/ASME Trans. Mechatronics*, vol. 28, no. 3, pp. 1337–1346, 2023.
- [21] Q. Zhao, J. Lai, K. Huang, X. Hu, and H. K. Chu, "Shape estimation and control of a soft continuum robot under external payloads," *IEEE/ASME Trans. Mechatronics*, vol. 27, no. 5, pp. 2511–2522, 2021.
- [22] J. Till, V. Aloj, and C. Rucker, "Real-time dynamics of soft and continuum robots based on Cosserat rod models," *Int. J. Rob. Res.*, vol. 38, no. 6, pp. 723–746, 2019.
- [23] F. Renda *et al.*, "A geometric variable-strain approach for static modeling of soft manipulators with tendon and fluidic actuation," *IEEE Rob. Autom. Lett.*, vol. 5, no. 3, pp. 4006–4013, 2020.
- [24] T. M. Bieze *et al.*, "Finite element method-based kinematics and closed-loop control of soft, continuum manipulators," *Soft Rob.*, vol. 5, no. 3, pp. 348–364, 2018.
- [25] J. Wang *et al.*, "A novel miniature spring-based continuum manipulator for minimally invasive surgery: Design and evaluation," *IEEE/ASME Trans. Mechatronics*, pp. 1–12, 2023.
- [26] B. Jones and I. Walker, "Kinematics for multisection continuum robots," *IEEE Trans. Robot.*, vol. 22, no. 1, pp. 43–55, 2006.
- [27] A. D. Marchese and D. Rus, "Design, kinematics, and control of a soft spatial fluidic elastomer manipulator," *Int. J. Rob. Res.*, vol. 35, no. 7, pp. 840–869, 2016.
- [28] C. Della Santina, R. K. Katzschmann, A. Bicchi, and D. Rus, "Model-based dynamic feedback control of a planar soft robot: Trajectory tracking and interaction with the environment," *Int. J. Rob. Res.*, vol. 39, no. 4, pp. 490–513, 2020.
- [29] Z. Gong *et al.*, "A soft manipulator for efficient delicate grasping in shallow water: Modeling, control, and real-world experiments," *Int. J. Rob. Res.*, vol. 40, no. 1, pp. 449–469, 2021.
- [30] D. C. Rucker and R. J. Webster, "Computing Jacobians and compliance matrices for externally loaded continuum robots," in *Proc. IEEE Int. Conf. Robot. Autom.*, 2011, pp. 945–950.
- [31] D. Lin *et al.*, "Position and orientation control of multissection magnetic soft microcatheters," *IEEE/ASME Trans. Mechatronics*, pp. 1–12, 2022.
- [32] E. Spyros-Papastavridis and J. S. Dai, "Flexible-joint humanoid balancing augmentation via full-state feedback variable impedance control," *J. Mech. Rob.*, vol. 13, no. 2, p. 021014, 2021.
- [33] J. Zhou *et al.*, "Bioinspired soft wrist based on multicable jamming with hybrid motion and stiffness control for dexterous manipulation," *IEEE/ASME Trans. Mechatronics*, vol. 28, no. 3, pp. 1256–1267, 2023.
- [34] G. Fang *et al.*, "Efficient Jacobian-based inverse kinematics with sim-to-real transfer of soft robots by learning," *IEEE/ASME Trans. Mechatronics*, vol. 27, no. 6, pp. 5296–5306, 2022.
- [35] E. Almanzor *et al.*, "Static shape control of soft continuum robots using deep visual inverse kinematic models," *IEEE Trans. Robot.*, vol. 39, no. 4, pp. 2973–2988, 2023.
- [36] Q. Fang *et al.*, "Soft lightweight small-scale parallel robot with high-precision positioning," *IEEE/ASME Trans. Mechatronics*, pp. 1–12, 2023.
- [37] X. Huang, J. Zou, and G. Gu, "Kinematic modeling and control of variable curvature soft continuum robots," *IEEE/ASME Trans. Mechatronics*, vol. 26, no. 6, pp. 3175–3185, 2021.
- [38] M. Li, R. Kang, D. T. Branson, and J. S. Dai, "Model-free control for continuum robots based on an adaptive kalman filter," *IEEE/ASME Trans. Mechatronics*, vol. 23, no. 1, pp. 286–297, 2017.
- [39] J. Nocedal and S. J. Wright, *Numerical optimization*. Springer, 2006.
- [40] J. Shi *et al.*, "Characterisation and control platform for pneumatically driven soft robots: Design and applications," in *Proc. IEEE Int. Conf. Soft Robot.*, 2023, pp. 1–8.
- [41] T. Greigarn, N. L. Poirot, X. Xu, and M. C. Çavuşoğlu, "Jacobian-based task-space motion planning for MRI-actuated continuum robots," *IEEE Rob. Autom. Lett.*, vol. 4, no. 1, pp. 145–152, 2019.
- [42] X. Huang, X. Zhu, and G. Gu, "Kinematic modeling and characterization of soft parallel robots," *IEEE Trans. Robot.*, vol. 38, no. 6, pp. 3792–3806, 2022.
- [43] P. Polygerinos *et al.*, "Modeling of soft fiber-reinforced bending actuators," *IEEE Trans. Robot.*, vol. 31, no. 3, pp. 778–789, 2015.
- [44] J. Till *et al.*, "Efficient computation of multiple coupled Cosserat rod models for real-time simulation and control of parallel continuum manipulators," in *Proc. IEEE Int. Conf. Robot. Autom.*, 2015, pp. 5067–5074.
- [45] G. Fang *et al.*, "Soft robotic manipulator for intraoperative MRI-guided transoral laser microsurgery," *Sci. Robot.*, vol. 6, no. 57, p. eabg5575, 2021.
- [46] F. Campisano *et al.*, "Closed-loop control of soft continuum manipulators under tip follower actuation," *Int. J. Rob. Res.*, vol. 40, no. 6–7, pp. 923–938, 2021.



**Jialei Shi** (Student Member, IEEE) received the B.S. degree from the Harbin Institute of Technology, China, in 2017, and the M.S. degree from the Beijing Institute of Technology, China, in 2019. During 2018–2019, he was a visiting student at Tsinghua University, China. He is currently pursuing the Ph.D degree in Mechanical Engineering at University College London, UK. His research interests include design, modelling and control of soft robots.



**Sara-Adela Abad** (Member, IEEE) is a Lecturer in Robotics at the Mechanical Engineering Department, University College London, UK. In 2019, she received her PhD degree in robotics from Imperial College London, UK. Her MSc degree in AI is from the University of Southampton, UK, and her BEng degree in electronic and control engineering is from the National Polytechnic School, Ecuador. Her research interests include bioinspiration, adaptability to uncertain conditions, and compliant robotics.



**Jian S Dai** (Fellow, IEEE) received a PhD degree in advanced kinematics and robotics from the University of Salford, UK, in 1993. He leads research in mechanisms and robotics with focus on kinematics, screw theory, metamorphic mechanisms, reconfigurable mechanisms and robotics. He is Fellow of the Royal Academy of Engineering, Member of Academia Europaea and has contributed over 500 publications. He was presented with the ASME Machine Design Award as the 58th recipient since the inception of the Award in 1958.



**Helge A. Wurdemann** (Member, IEEE) is Professor of Robotics at University College London, leading robotics in the Department of Mechanical Engineering. He received a degree (Dipl.-Ing.) in electrical engineering with a focus on mechatronics and robotics in the medical field from the Leibniz University of Hanover, and a PhD in Robotics from King's College London in 2012. Helge has authored over 100 articles, published in high-impact journals, and peer-reviewed full-length conference papers.

# Supplementary Material for Position and Orientation Control for Hyperelastic Multisegment Continuum Robots

Jialei Shi, *Student Member, IEEE*, Sara-Adela Abad, *Member, IEEE*, Jian Sheng Dai, *Fellow, IEEE*, Helge A Wurdemann, *Member, IEEE*

This document includes the supplementary details for low-level pressure control (see Section S.I), constructing the rotation error  $e_R$  solving the optimisation problem (see Section S.II and Equation (17) in the manuscript), numerical investigation of control accuracy and computational time (see Section S.III), and an uncertainties and sensitivity analysis (see Section S.IV). Please note "manuscript" refers to the main paper in this Supplementary Material.

## S.I. SUPPLEMENTARY DETAILS FOR THE CONTROL SCHEME

Fig. S1 illustrates the control scheme for inverse kinematics control. MATLAB (R2019a) is used to solve the optimisation problem and achieve inverse kinematics control. The experimental hardware is integrated to a control platform, as reported in [1]. Desired pressure from the inverse kinematics controller is converted to desired PWM signals and sent to the Arduino Due. MATLAB and Arduino communicate via the MATLAB Support Package for Arduino. The Arduino board then generates the PWM signals which are converted to 0 ~ 10 V control analogue signals. These control signals are received by the pressure regulators (Camozi K8P), which employ a built-in closed-loop controller to achieve pressure control. The analogue signal range of 0.4 ~ 9.5 V corresponds to a pressure range of 0 ~ 3 bar. The pressure regulators can send real pressure values to the Arduino board. The pressure regulators can send real pressure values to the Arduino board. An electromagnetic tracking system (NDI Aurora) monitors the tip position/orientation of Segment 1 and 2 via magnetic trackers, transmitting this information to MATLAB for data recording and processing.

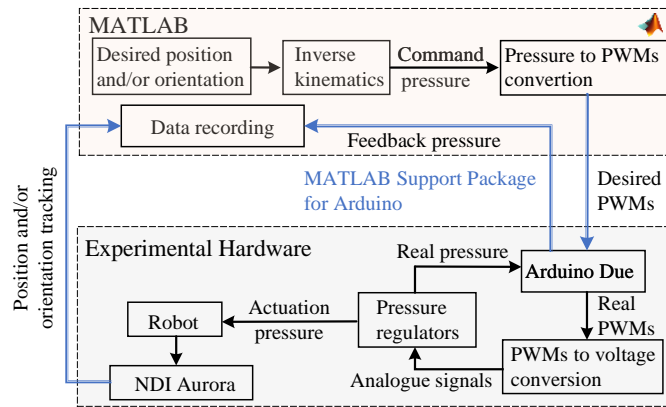


Fig. S1. Scheme for inverse kinematics control. MATLAB and the Arduino board communicate via the MATLAB Support Package for Arduino.

## S.II. SUPPLEMENTARY DETAILS FOR OPTIMISATION-BASED INVERSE KINEMATICS CONTROL

This section details the underlying theory of defining the rotation error of  $e_R = (R(t)^T R_d^t - R(t)(R_d^t)^T)^\vee$  in the optimisation problem, which is reported in (17) in the manuscript, to control the orientation.

$SO(3)$  is the special orthogonal group and  $SO(3) := \{R \in \mathbb{R}^{3 \times 3} | R^T R = I_{3 \times 3}, \det(R) = 1\}$ .  $R$  is the rotation matrix.  $\mathfrak{so}(3)$  is the Lie algebra of  $SO(3)$  [2]. To define the error between a desired rotation matrix and a simulated rotation matrix

Jialei Shi, Sara-Adela Abad and Helge A. Wurdemann are with the Department of Mechanical Engineering, University College London, UK. (e-mail: jialei.shi.19@ucl.ac.uk; h.wurdemann@ucl.ac.uk).

Sara-Adela Abad is also with the Institute for Applied Sustainability Research, Quito, Ecuador. (e-mail: s.abad-guaman@ucl.ac.uk);

Jian Sheng Dai is with the Institute for Robotics, Southern University of Science and Technology, Shenzhen, China and with the Centre for Robotics Research, Department of Engineering, King's College London, London, UK (e-mail: jian.dai@kcl.ac.uk).

for orientation control (see (17) in the manuscript), an error function  $e_R$  should achieve  $SO(3) \times SO(3) \rightarrow \mathbb{R}^3$ . Equation (1) in the manuscript introduces the operation  $(\hat{\cdot})$ , which is the mapping from  $\mathbb{R}^3$  to  $\mathfrak{so}(3)$  [3] and has the form in (S1).

$$\hat{a} = \begin{bmatrix} 0 & -a_3 & a_2 \\ a_3 & 0 & -a_1 \\ -a_2 & a_1 & 0 \end{bmatrix}. \quad (\text{S1})$$

For a matrix  $B \in \mathfrak{so}(3)$ , the inverse operation of  $(\hat{\cdot})$  is in (S2).

$$B^\vee = [B_{3,2}, B_{1,3}, B_{2,1}]^T = b, \quad (\text{S2})$$

where  $b$  is a vector and  $b \in \mathbb{R}^3$ .  $B_{i,j}$  denotes the value in the  $i$ th row and the  $j$ th column of the matrix  $B$ . As reported in the manuscript,  $R_d^t$  is the desired rotation matrix, and  $R(t)$  is the simulated matrix at the tip of soft robots from the kinematics model. The relative rotation matrix  $\Delta R$  from the  $R(t)$  to  $R_d^t$  is  $\Delta R = R(t)^T R_d^t$ . As  $\Delta R \in SO(3)$ , it has the form in (S3).

$$\Delta R = \begin{bmatrix} \Delta R_{1,1} & \Delta R_{1,2} & \Delta R_{1,3} \\ \Delta R_{2,1} & \Delta R_{2,2} & \Delta R_{2,3} \\ \Delta R_{3,1} & \Delta R_{3,2} & \Delta R_{3,3} \end{bmatrix}. \quad (\text{S3})$$

To define the rotation error  $e_R$  for optimisation,  $\Delta R$  needs to be expressed using angle-axis representation. The angle-axis representation is a non-minimal implementation of rotations, defined by an angle  $\theta$  and an axis vector  $n$ . The vector  $n \in \mathbb{R}^3$  defines the rotation direction, and  $\theta \in \mathbb{R}$  defines the rotation magnitude [2]. The matrix  $\Delta R$ , its equivalent angle  $\Delta\theta$  and axis  $n$  have the form in (S4).

$$n = \frac{1}{2\sin\Delta\theta} \begin{bmatrix} \Delta R_{3,2} - \Delta R_{2,3} \\ \Delta R_{1,3} - \Delta R_{3,1} \\ \Delta R_{2,1} - \Delta R_{1,2} \end{bmatrix}. \quad (\text{S4})$$

As such, the general form of the error matrix  $e_R$  can be defined as in (S5).

$$e_R = (\Delta R - \Delta R^T)^\vee = (R(t)^T R_d^t - (R_d^t)^T R(t))^\vee, \quad (\text{S5})$$

where  $e_R$  is a  $3 \times 1$  vector and  $e_R = 2\sin\Delta\theta \cdot n$ . In this way, the first and second items of  $e_R$  can be used as the rotation error for orientation control, so that the  $z$ -axis is constrained [4], [5] for achieving a bending angle control.

When the robot has a bending angle of  $\theta_d$  during trajectory tracking  $y_d = [x_d, y_d, z_d]$  (Experiment 3),  $R_d^t$  is expressed in (S6).

$$R_d^t = [n_x^T \ n_y^T \ n_z^T]^T, \quad (\text{S6})$$

where  $n_x$ ,  $n_y$  and  $n_z$  are directional vectors along the  $x$ -,  $y$ - and  $z$ -axes, respectively. They can be defined as in (S7).

$$\begin{aligned} n_x &= [\cos \beta \cos \theta_d, \sin \beta \cos \theta_d, \sin \theta_d], \\ n_y &= [-\sin \beta, \cos \beta, 0], \quad \beta = \text{atan2}(y_d^t, x_d^t), \\ n_z &= [\sin \theta_d \cos \beta, \sin \theta_d \sin \beta, \cos \theta_d]. \end{aligned} \quad (\text{S7})$$

In this way,  $n_z = [0, 0, 1]$  when the desired bending angle  $\theta_d$  is  $0^\circ$ . Combining (S5) - (S7), the analytical form of  $e_R$  used in the optimisation problem of (17) is a  $2 \times 1$  vector and is described by (S8).

$$e_R = \begin{bmatrix} R(t)_{2,3} \cos \beta - R(t)_{1,3} \sin \beta - R(t)_{3,2} \cos \theta_d - R(t)_{1,2} \cos \beta \sin \theta_d - R(t)_{2,2} \sin \beta \sin \theta_d \\ R(t)_{3,1} \cos \theta_d + R(t)_{3,3} \sin \theta_d - R(t)_{1,3} \cos \beta \cos \theta_d + R(t)_{1,1} \cos \beta \sin \theta_d - R(t)_{2,3} \sin \beta \cos \theta_d + R(t)_{2,1} \sin \beta \sin \theta_d \end{bmatrix}. \quad (\text{S8})$$

Equation (S8) explicitly describes  $e_R$  when the desired bending angle is  $\theta_d$ , while the desired position vector  $y_d^t$  is  $[x_d^t, y_d^t, z_d^t]^T$ . When  $e_R$  is nullified, bending angle control is achieved.

### S.III. NUMERICAL COMPARISON BETWEEN CONTROL ACCURACY AND COMPUTATIONAL TIME

This section involves numerical computations aimed at investigating the relationship between control accuracy and computation time. Specifically, this section implements tip position and orientation control of a two-segment robot (refer to (17) in the manuscript). The objective is to control the overall robot tip to follow a circular trajectory with a radius of 50 mm, while maintaining a bending angle of  $60^\circ$ . The termination tolerance of the sum of squared residual errors is set as  $10^{-1}$ ,  $10^{-3}$ ,  $10^{-6}$ ,  $10^{-9}$ ,  $10^{-12}$  when solving the optimisation problem. The simulations are conducted using MATLAB on a PC equipped with an Intel i5 processor and 32 GB RAM. The outcomes of the simulations are presented in Fig. S2.

Fig. S2(a) demonstrates the simulation results when the termination tolerance is set as  $10^{-6}$ , and  $10^{-6}$  is adopted in the manuscript. Fig. S2(b) illustrates that the computational time increases with the decrease of the termination tolerance. For instance, the computational time is approximately 0.08 s and 0.105 s when the tolerance is  $10^{-6}$  and  $10^{-12}$ , respectively. Fig. S2(c) shows that the average tip position tracking error converges when the tolerance is smaller than  $10^{-6}$ . Similarly, the angle control errors are observed to start to converge when the termination tolerance is  $10^{-6}$ , as reported in Fig. S2(d).

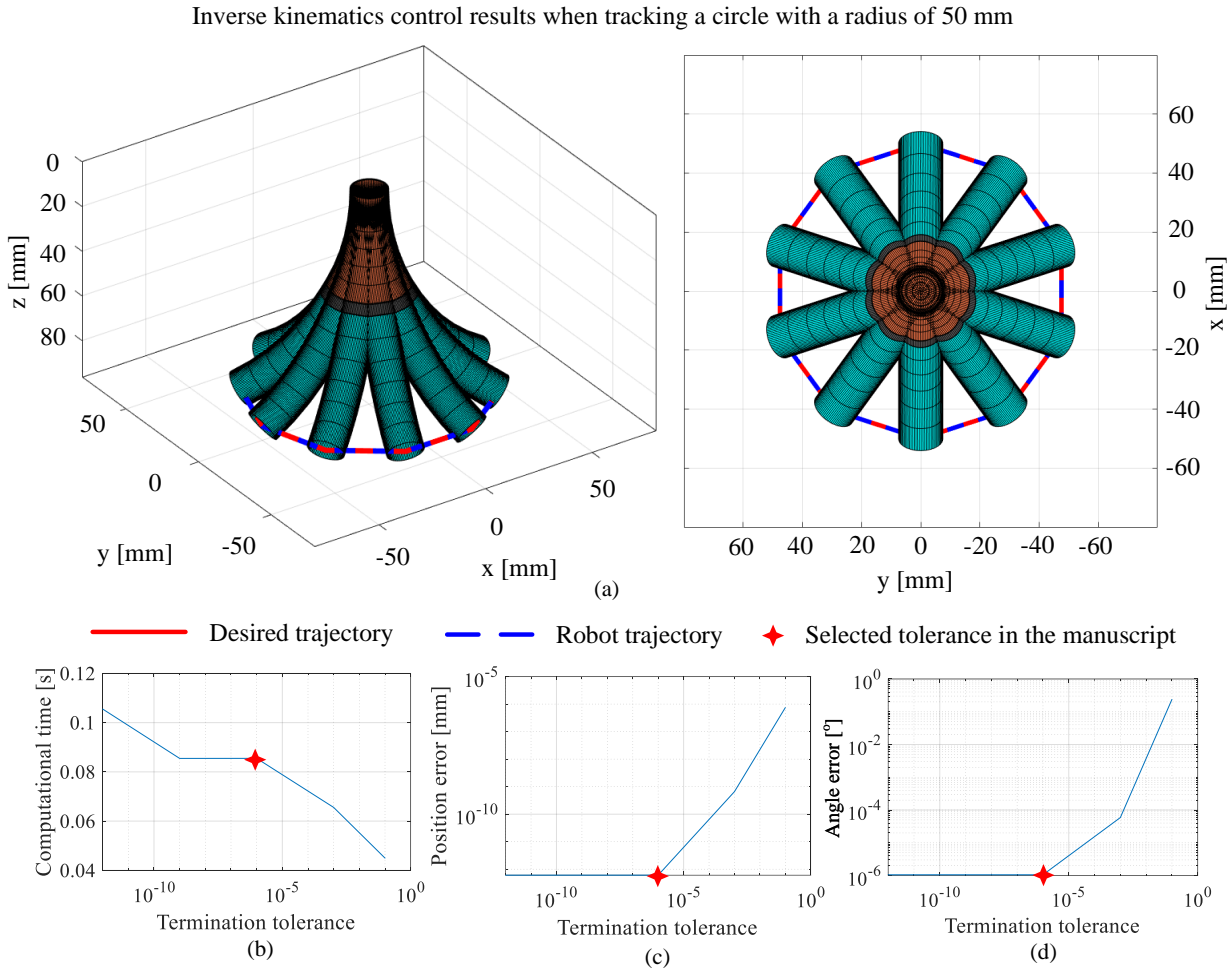


Fig. S2. (a) Inverse kinematics control results when the overall tip of a two-segment robot tracks a circle with a radius of 50 mm, with a tip bending angle of 60°. (b) Computational time, (b) average tip position control errors, and (c) average tip bending angle errors versus termination tolerance.

In summary, opting for a termination tolerance smaller than  $10^{-6}$  leads to an escalation in computational time without enhancements in accuracy. Consequently, for the sake of striving for a balance between error convergence and computational efficiency,  $10^{-6}$  is chosen in the manuscript.

In addition, simulations have been conducted to investigate any error propagation from the first robot segment (Segment 1) to the second robot segment (Segment 2). The desired tip trajectory and tip bending angle settings are chosen as the ones shown in Figure. 2(a). The simulation results are summarised in Table SI. Table SI demonstrates that the midpoint position errors might propagate to the overall tip and introduce errors to the overall tip control. For instance, when the midpoint errors are between 0.4 - 1.6 mm, the propagated overall tip position control errors increase to 1.2 - 4.6 mm. Moreover, the midpoint position control errors also contribute to bending angle control errors at the overall tip of soft robots, demonstrated by the last column in Table SI.

#### S.IV. SUPPLEMENTARY DETAILS FOR THE UNCERTAINTIES AND SENSITIVITY ANALYSIS

To perform an uncertainties and sensitivity analysis for our approach, we included uncertainties introduced by the robot length  $L$ , cross-sectional area  $A$ , second moment of area  $I$ , modulus  $E$  as well as measurement uncertainties from the controlled

TABLE SI  
SIMULATION RESULTS OF CONTROL ERROR PROPAGATION FROM THE SEGMENT 1 TO SEGMENT 2

Average midpoint control error [mm]	Average propagated overall tip control error [mm]	Average propagated tip bending angle control error [°]
0.4	1.2	1.1
0.8	2.1	1.7
1.2	3.4	2.9
1.6	4.6	4.0

TABLE SII  
ANALYSIS OF MODELLING AND MEASUREMENT UNCERTAINTIES

	Moduli fitting	Pressure control	Position measurement	Angle measurement
Errors	$\pm 63.73 \text{ Pa}$ (Segment 1), $\pm 35.8 \text{ Pa}$ (Segment 2).	$\pm 0.03 \text{ bar}$	$\pm 0.48 \text{ mm}$	$\pm 0.30^\circ$
Uncertainties	One-chamber-pair actuation Tip position [mm], Bending angle [°]	Two-chamber-pair actuation Tip position [mm], Bending angle [°]	Three-chamber-pair actuation Tip position [mm], Bending angle [°]	
Robot length ( $L$ )	-5% (-33.8 + 0.7, 0, 4.5 + 1.9), 171.4 - 7.8 -2.5% (-33.8 + 0.3, 0, 4.5 + 1.0), 171.4 - 3.9 0% (-33.8, 0, 4.5), 171.4 2.5% (-33.8 - 0.3, 0, 4.5 - 0.9), 171.4 + 3.8 5% (-33.8 - 0.4, 0, 4.5 - 1.9), 171.4 + 7.7	(-6.5 - 1.6, -11.2 - 2.9, -10.7 - 0.2), 276.8 - 14.7 (-6.5 - 0.8, -11.2 - 1.4, -10.7 - 0.2), 276.8 - 7.1 (-6.5, -11.2, -10.7), 276.8 (-6.5 + 0.8, -11.2 + 1.3, -10.7 + 0.4), 276.8 + 7.0 (-6.5 + 1.6, -11.2 + 2.7, -10.7 + 1), 276.8 + 14.5	(0, 0, 81.4 - 4.1), 0 (0, 0, 81.4 - 2.0), 0 (0, 0, 81.4), 0 (0, 0, 81.4 + 2.0), 0 (0, 0, 81.4 + 4.1), 0	
Cross-section Area ( $A$ )	-5% (-33.8 - 0.1, 0, 4.5 - 0.6), 171.4 + 2.0 -2.5% (-33.8 - 0.1, 0, 4.5 - 0.3), 171.4 + 1.0 0% (-33.8, 0, 4.5), 171.4 2.5% (-33.8 - 0.0, 0, 4.5 + 0.3), 171.4 - 1.0 5% (-33.8 - 0.0, 0, 4.5 + 0.6), 171.4 - 1.9	(-6.5 + 0.8, -11.2 + 1.3, -10.7 + 0.2), 276.8 + 6.4 (-6.5 + 0.4, -11.2 + 0.6, -10.7 + 0.0), 276.8 + 3.0 (-6.5, -11.2, -10.7), 276.8 (-6.5 - 0.3, -11.2 - 0.6, -10.7 - 0.1), 276.8 - 3.0 (-6.5 - 0.9, -11.2 - 1.7, -10.7 - 0.1), 276.8 - 7.3	(0, 0, 81.4 + 2.1), 0 (0, 0, 81.4 + 1.0), 0 (0, 0, 81.4), 0 (0, 0, 81.4 - 1.0), 0 (0, 0, 81.4 - 1.9), 0	
Second moment of area ( $I_x, I_y$ )	-5% (-33.8 + 1.4, 0, 4.5 - 2.7), 171.4 + 9.2 -2.5% (-33.8 + 0.6, 0, 4.5 - 1.3), 171.4 + 4.5 0% (-33.8, 0, 4.5), 171.4 2.5% (-33.8 - 0.6, 0, 4.5 + 1.3), 171.4 - 4.2 5% (-33.8 - 1.1, 0, 4.5 + 2.6), 171.4 - 8.2	(-6.5 + 2.1, -11.2 + 3.5, -10.7 + 1.4), 276.8 + 16.2 (-6.5 + 1.1, -11.2 + 1.8, -10.7 + 0.6), 276.8 + 8.0 (-6.5, -11.2, -10.7), 276.8 (-6.5 - 1.1, -11.2 - 2.0, -10.7 - 0.4), 276.8 - 8.0 (-6.5 - 2.1, -11.2 - 3.7, -10.7 - 0.5), 276.8 - 14.6	(0, 0, 81.4), 0 (0, 0, 81.4), 0 (0, 0, 81.4), 0 (0, 0, 81.4), 0 (0, 0, 81.4), 0	
Modulus $E$	-5% (-33.8 + 1.4, 0, 4.5 - 3.1), 171.4 + 10.9 -2.5% (-33.8 + 0.6, 0, 4.5 - 1.0), 171.4 + 5.3 0% (-33.8, 0, 4.5), 171.4 2.5% (-33.8 - 0.6, 0, 4.5 + 1.3), 171.4 - 4.2 5% (-33.8 - 1.1, 0, 4.5 + 2.6), 171.4 - 8.2	(-6.5 + 2.6, -11.2 + 4.5, -10.7 + 2.0), 276.8 + 22.1 (-6.5 + 1.4, -11.2 + 2.3, -10.7 + 0.8), 276.8 + 10.9 (-6.5, -11.2, -10.7), 276.8 (-6.5 - 1.3, -11.2 - 2.4, -10.7 - 0.4), 276.8 - 9.9 (-6.5 - 2.7, -11.2 - 4.7, -10.7 - 0.4), 276.8 - 14.6	(0, 0, 81.4 + 2.1), 0 (0, 0, 81.4 + 1.0), 0 (0, 0, 81.4), 0 (0, 0, 81.4 - 1.0), 0 (0, 0, 81.4 - 1.9), 0	
Pressure $P$	-5% (-33.8 - 1.2, 0, 4.5 + 4.2), 171.4 - 13.3 -2.5% (-33.8 - 0.7, 0, 4.5 + 2.1), 171.4 - 6.7 0% (-33.8, 0, 4.5), 171.4 2.5% (-33.8 + 0.9, 0, 4.5 - 2.5), 171.4 + 7.0 5% (-33.8 + 2.0, 0, 4.5 - 4.0), 171.4 + 14.1	(-6.5 - 3.9, -11.2 - 6.8, -10.7 - 0.1), 276.8 - 27.9 (-6.5 - 1.8, -11.2 - 3.2, -10.7 - 0.4), 276.8 - 12.8 (-6.5, -11.2, -10.7), 276.8 (-6.5 + 1.7, -11.2 + 2.9, -10.7 + 1.0), 276.8 + 13.8 (-6.5 + 3.2, -11.2 + 5.5, -10.7 + 2.7), 276.8 + 27.9	(0, 0, 81.4 - 2.3), 0 (0, 0, 81.4 - 1.2), 0 (0, 0, 81.4), 0 (0, 0, 81.4 + 1.2), 0 (0, 0, 81.4 + 2.3), 0	

For one-chamber-pair actuation,  $P^1 = P^2 = 1.5 \text{ bar}$ . For two-chamber-pair actuation  $P^1 = P^2 = P^3 = P^4 = 1.5 \text{ bar}$ . For three-chamber-pair actuation,  $P^1 \sim P^6 = 1.5 \text{ bar}$ .

pressure  $P$  and measured position and orientation from the magnetic sensors  $M$ . As such, the result  $r$  can be described by (S9).

$$r = r(L, A, I, E, P, M). \quad (\text{S9})$$

Table SII summaries the uncertainties from moduli fitting, pressure control, position and angle measurement. To further conduct a general sensitivity analysis, we adopt the Taylor Series Method (TSM). For more detail, the theory is reported in [6], [7]. The combined standard uncertainty  $u_r$  in (S9) is given by (S10).

$$u_r^2 = \left( \frac{\partial r}{\partial L} \right)^2 u_L^2 + \left( \frac{\partial r}{\partial A} \right)^2 u_A^2 + \left( \frac{\partial r}{\partial I} \right)^2 u_I^2 + \left( \frac{\partial r}{\partial E} \right)^2 u_E^2 + \left( \frac{\partial r}{\partial P} \right)^2 u_P^2 + \left( \frac{\partial r}{\partial M} \right)^2 u_M^2, \quad (\text{S10})$$

where  $u_L, u_A, u_I, u_E, u_P, u_M$  are the uncertainties for  $L, A, I, E, P$  and  $M$ . To normalise (S10), an uncertainty percentage contribution (UPC) can be calculated to determine the percentage contribution of each uncertainty to the overall squared sum of uncertainties [6]. For instance, the UPC of robot length is defined in (S11).

$$\text{UPC}_L = \frac{\left( \frac{\partial r}{\partial L} \right)^2 u_L^2}{u_r^2}. \quad (\text{S11})$$

Following the TSM, we considered uncertainties of -5%, -2.5%, 2.5% and 5%. Based on (S10), Table 3 reports on the resulting uncertainties of tip position and bending angle for Segment 1. Combining Table S3 and (S11), the UPC values are presented in Fig. S3.

Fig. S3(a) reports on the UPC values with respect to the tip positions. The results show that the pressure uncertainty contributes to about 40% to 60% of the overall uncertainties of the tip position. The modulus and second moment of area have similar uncertainty contributions, with UPC values of 15% ~ 25%. In all cases, the UPC of the robot length is around 10%. The combination of cross-sectional area and measurement only contributes to less than 4% uncertainties of the tip position. In contrast, when the robot elongates, the robot length becomes the dominant factor contributing to over 50% of the tip position uncertainties. The UPC values for cross-sectional area, modulus, and pressure range from 15% to 20%. Meanwhile, the second moment of area has no influence on the robot's elongation error.

Fig. S3(b) illustrates that the pressure uncertainty brings 40% ~ 50% uncertainties of the bending angle. Moreover, the uncertainties in robot length, second moment of area, and modulus, represented by the UPC values, range from 15% to 30%. Similar to the tip position analysis, the combined effect of cross-sectional area and measurement uncertainties is below 4%.

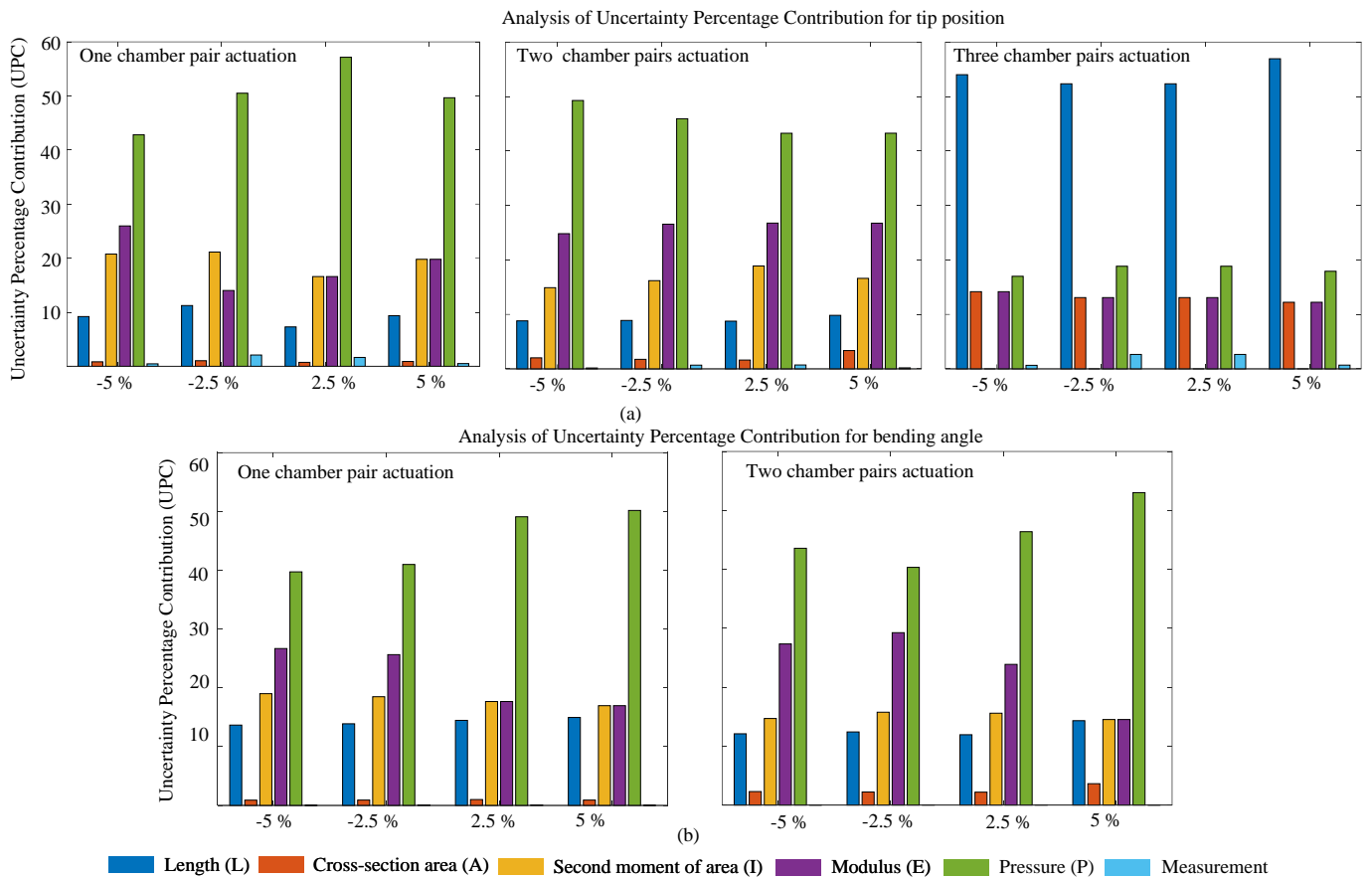


Fig. S3. Analysis of uncertainty percentage contribution with regards to the (a) tip position and (b) tip bending angle, where uncertainties in the robot length, cross-sectional area, second moment of area, modulus, actuation pressure and sensor measurement are included.

In summary, the analysis reveals that precise pressure control is crucial for effective model-based control. In our study, the uncertainty associated with pressure control is less than 1% of the full-scale pressure, as indicated in Table S3. Furthermore, the findings demonstrate that the selected tracking sensor has minimal impact on the overall results. Additionally, we have successfully identified the dynamic modulus through experiments, thereby reducing the overall uncertainties in the modelling process.

## REFERENCES

- [1] J. Shi, W. Gaozhang, H. Jin, G. Shi, and H. Wurdemann, "Characterisation and control platform for pneumatically driven soft robots: Design and applications," in *Proc. IEEE Int. Conf. Soft Robot.*, 2023, pp. 1–8.
- [2] M. Spong, S. Hutchinson, and M. Vidyasagar, *Robot Modeling and Control*. Wiley, 2005.
- [3] J. Till, V. Alois, and C. Rucker, "Real-time dynamics of soft and continuum robots based on Cosserat rod models," *Int. J. Rob. Res.*, vol. 38, no. 6, pp. 723–746, 2019.
- [4] R. Mahony, V. Kumar, and P. Corke, "Multirotor aerial vehicles: Modeling, estimation, and control of quadrotor," *IEEE Rob. Autom. Mag.*, vol. 19, no. 3, pp. 20–32, 2012.
- [5] J. Till, C. E. Bryson, S. Chung, A. Orekhov, and D. C. Rucker, "Efficient computation of multiple coupled Cosserat rod models for real-time simulation and control of parallel continuum manipulators," in *Proc. IEEE Int. Conf. Robot. Autom.*, 2015, pp. 5067–5074.
- [6] H. W. Coleman and W. G. Steele, *Experimentation, Validation, and Uncertainty Analysis for Engineers*. John Wiley & Sons, 2018.
- [7] R. Benedict, "ASME measurement uncertainty," *J. Fluids Eng.*, vol. 107, p. 161, 1985.